



General-relativistic Bondi-Hoyle-Lyttleton accretion in a toroidally magnetized medium

Yoonsoo Kim ^{1,2,*} and Elias R. Most ^{1,3}

¹*Theoretical Astrophysics 350-17, California Institute of Technology, Pasadena, California 91125, USA*

²*Department of Physics, California Institute of Technology, Pasadena, California 91125, USA*

³*Walter Burke Institute for Theoretical Physics, California Institute of Technology, Pasadena, California 91125, USA*

(Dated: September 20, 2024)

The dynamics of a black hole traveling through a plasma – a general relativistic extension of the classic Bondi-Hoyle-Lyttleton (BHL) accretion problem – can be related to a variety of astrophysical contexts, including the aftermath of binary black hole mergers in gaseous environments. We perform three-dimensional general relativistic magnetohydrodynamics simulations of BHL accretion onto a rotating black hole for an incoming flow with a toroidal (inclined) magnetization with respect to the spin axis of the black hole. Irrespective of inclination but dependent on the wind speed, we find that the accretion flow onto the black hole can become magnetically arrested, launching an intermittent (and sometimes striped) jet. The upstream ram pressure of the wind bends the jet, and confines the angular extent into which the magnetic flux tubes ejected from quasi-periodic eruptions are released. Recoil from magnetic flux eruptions drives strong oscillations in the accretion plane, resulting in jet nutation at the outer radii and occasionally ripping off the inner part of the accretion disk. In addition to dynamical friction, the black hole experiences a perpendicular drag force analogous to the Magnus effect. Qualitative effects of the incoming magnetic field orientation, the strength of the magnetization, and the incoming wind speed are investigated as well.

I. INTRODUCTION

A. BBH merger remnant in AGN disk

The merger of a binary black hole (BBH) [1–4] within the accretion disk of an active galactic nucleus (AGN) [5–11] is thought to be one of major channels of the observed BBH mergers, but is also an interesting astrophysical scenario within the context of multi-messenger astronomy. If asymmetry is present in a black hole binary, the resulting anisotropic emission of gravitational waves from the merger can impart a recoil onto the post-merger remnant black hole (BH) [12, 13]. Since the kicked remnant will be moving through a gas-rich environment, a luminous accretion flow onto or a relativistic jets from the BH may give rise to an observable post-merger electromagnetic signal [14, 15].

The gaseous environment of the AGN disk can affect the long-term evolution of an embedded BBH, often putting constraints on its orbital configuration. Newtonian studies suggest that orbital and spin axes of a BBH embedded in a gaseous environment align over time [16, 17], and the orbit is driven to be aligned with the AGN disk plane as well [18]. These findings, put together, indicate that both the orbital angular momentum and spin of the BBH are likely aligned with the AGN disk. Unless anisotropic gravitational radiation induces a significant torque on the system, the remnant would retain its prior spin direction.

Recent large-scale cosmological simulations revealed that the magnetic field of AGN disks are predominantly

toroidal (parallel to the accretion plane)[19, 20]. The presence of mixed poloidal-toroidal configurations is also in line with simulations of magnetized circumbinary disks around BBHs [21]. This motivates a theoretical investigation on a recoiled black hole flying through a plasma with a toroidal magnetization of varying inclination relative to the spin of the black hole.

B. Bondi-Hoyle-Lyttleton accretion

Bondi-Hoyle-Lyttleton (BHL) accretion [22, 23] is a classic problem in astrophysics involving a gravitational accretor traveling through a uniform fluid. Despite being highly simplified, it can be applied to a wide range of astrophysical systems including common envelope phases of binary star evolution [24–27], wind-fed X-ray binaries [28], star clusters [29] or protoplanetary disks [30]. Owing to its astrophysical significance, a large volume of analytical and numerical studies exist in the literature on Newtonian [see 31, 32, for a review] and relativistic [33–53] regimes.

Basic physical scales associated with BHL accretion are the accretion radius¹

$$R_a = \frac{2GM}{v_\infty^2}, \quad (1)$$

¹ An alternate definition of the accretion radius exists in the literature

$$R_a = \frac{2GM}{c_{s,\infty}^2 + v_\infty^2},$$

where $c_{s,\infty}$ is the asymptotic sound speed of the incoming fluid. We adopt the definition (1) throughout this paper.

* ykim7@caltech.edu

the accretion timescale

$$\tau_a = \frac{R_a}{v_\infty} = \frac{2GM}{v_\infty^3}, \quad (2)$$

and the Bondi-Hoyle-Lyttleton mass accretion rate

$$\dot{M}_{\text{BHL}} = \pi R_a^2 \rho_\infty v_\infty = \frac{4\pi G^2 M^2 \rho_\infty}{v_\infty^3}, \quad (3)$$

where G is the gravitational constant, M is the mass of the accreting object, v_∞ is the asymptotic relative velocity, and ρ_∞ is the asymptotic mass density of the fluid.

A major challenge in computational approaches to this problem is its inherent multi-scale nature, namely simultaneously resolving the size of the accreting object r_0 and the accretion radius R_a on a single numerical grid. For example, a black hole with mass M has $r_0 \approx r_g$ where

$$r_g = \frac{GM}{c^2} \quad (4)$$

is the gravitational radius of the black hole. The ratio between the two length scales is

$$\frac{R_a}{r_g} \sim \left(\frac{v_\infty}{c}\right)^{-2}. \quad (5)$$

Also, time integration needs to be performed at least several times of τ_a to reach a steady state, which is longer than the dynamical timescale associated with the black hole by a factor of

$$\frac{\tau_a}{(r_g/c)} \sim \left(\frac{v_\infty}{c}\right)^{-3}. \quad (6)$$

A large separation in both length (5) and time (6) scales, which is especially severe for a compact accretor such as a black hole, rapidly increases the computational cost for realistic values of v_∞ . As a result, many studies are often forced to assume an unrealistically fast velocity of the BH relative to the fluid. Due to its high computational cost, most numerical studies on general relativistic BHL accretion have considered hydrodynamic flows on either 2D planar or 3D axisymmetric geometry [36–49]. However, inclusion of magnetic fields can dramatically alter the flow morphology, and a restrictive nature of the assumed spatial symmetry might fail to fully capture multi-dimensional effects. Following the first study in 2D MHD [50] and of 3D hydrodynamic flow [51], the first simulations of GRMHD Bondi-Hoyle-Lyttleton accretion in full 3D have been carried out only recently [52, 53]. Each of these studies respectively explored jet launching from the BH [52] and the effect of the BH spin-wind orientation on the shock morphology [53], which can only be properly captured in a 3D MHD simulation.

In this paper, we perform general relativistic magnetohydrodynamics (GRMHD) simulations of a spinning black hole traveling through a fluid with a toroidal (inclined) magnetic field relative to the spin axis of the BH.

The physical scenario is approximated by a relativistic Bondi-Hoyle-Lyttleton accretion problem with a magnetized wind. We examine large-scale morphology and temporal evolution of the accretion flow, both of which are closely related to intermittent jet launching and magnetic flux eruptions from the BH. The impacts of magnetic field orientation, magnetization, and the wind speed are assessed by systematically varying simulation parameters.

Another purpose of our numerical experiment is to measure the jet luminosity (power) and determine the efficiency with which $\dot{M}_{\text{BHL}}c^2$ can be converted into a jet luminosity. The drag force exerted on the accreting BH is also measured and its astrophysical implications are discussed.

This article is organized as follows. In Sec. II, we describe our numerical setup and methods. We present our results in two steps, focusing on a specific parameter set first in Sec. III, before generalizing it in Sec. IV. We present discussions on the results in Sec. V, then summarize our main findings along with limitations and future perspectives in Sec. VI.

II. METHODS

The background spacetime is set to the Kerr metric in (Cartesian) Kerr-Schild coordinates. The spin of the black hole is aligned with the \hat{z} axis of the computational domain. The exact form of the spacetime metric in these coordinates is

$$ds^2 = -dt^2 + dx^2 + dy^2 + dz^2 + \frac{2Mr^3}{r^4 + a^2z^2} \times \left[dt + \frac{r(xdx + ydy) + a(ydx - xdy)}{r^2 + a^2} + \frac{zdz}{r} \right]^2, \quad (7)$$

where M is the mass and $a \equiv J/M$ is the spin parameter of the black hole. The coordinate variable r is defined as

$$\frac{x^2 + y^2}{r^2 + a^2} + \frac{z^2}{r^2} = 1. \quad (8)$$

We solve the equations of ideal GRMHD, which are given in terms of the rest-mass density current

$$J^\mu = \rho u^\mu, \quad (9)$$

and the stress-energy tensor,

$$T^{\mu\nu} = (\rho + e + p + b^2) u^\mu u^\nu + \left(P + \frac{b^2}{2} \right) g^{\mu\nu} - b^\mu b^\nu, \quad (10)$$

with its electromagnetic component

$$T_{\text{EM}}^{\mu\nu} = b^2 u^\mu u^\nu + \frac{b^2}{2} g^{\mu\nu} - b^\mu b^\nu, \quad (11)$$

where ρ is the rest mass density, e is the internal energy density, p is the pressure, u^μ is the four-velocity, and b^μ

the comoving magnetic field of the fluid, with $b^2 = b^\mu b_\mu$. The electromagnetic field is evolved using the dual field strength tensor,

$$*F^{\mu\nu} = b^\mu u^\nu - u^\mu b^\nu. \quad (12)$$

The evolution equations are

$$\nabla_\mu J^\mu = 0, \quad (13)$$

$$\nabla_\mu *F^{\mu\nu} = 0, \quad (14)$$

$$\nabla_\mu T^{\mu\nu} = 0. \quad (15)$$

We find it advantageous to define a normal magnetic field as²

$$\bar{B}^i = *F^{0i}. \quad (16)$$

We further model the gas dynamics using an ideal fluid equation of state

$$p = e(\Gamma - 1), \quad (17)$$

where $\Gamma = 5/3$ is the adiabatic index.

A. Numerical setup

We numerically solve the ideal GRMHD system using ATHENAK³ code, a rewrite of the ATHENA++ [57] using the performance portability library Kokkos [58].

The computational domain $[-40960r_g, 40960r_g]^3$ is discretized into a uniform Cartesian grid with the base grid resolution 256^3 . 13 levels of static mesh refinement are applied around the coordinate origin, with the innermost mesh $[-5r_g, 5r_g]^3$ providing a resolution of ~ 26 grid points per r_g . Time integration is performed using a second order Runge-Kutta stepper, piecewise parabolic reconstruction [59], an HLLC Riemann solver [60, 61], and a constrained transport algorithm [62]. We use the mass density and internal energy floor values $\rho_{\text{floor}} = 10^{-14}\rho_\infty$, $e_{\text{floor}} = \rho_{\text{floor}}c^2/3$, and cap the maximum Lorentz factor of the fluid to $W_{\text{max}} = 20$. The drift frame flooring technique [63] is applied to limit the comoving magnetization to $\sigma_{\text{max}} = 50$.

ATHENAK can be compiled and run on graphics processing unit (GPU) devices at scale, providing $\mathcal{O}(10^7)$ cell updates per second per each GPU card for large

scale GRMHD simulations. The simulations presented here overall have been performed on 132 GPU nodes (792 NVIDIA Volta cards) at OLCF Summit cluster, costing 900 node hours per $10^4 r_g/c$ integration time on average. The total computational cost used for all simulations is about 34,000 node hours.

B. Initial data

The upstream wind is initialized with a uniform rest mass density ρ_∞ and spatial velocity

$$u^{i'} = \left(-\frac{v_\infty}{\sqrt{1 - v_\infty^2/c^2}}, 0, 0 \right), \quad (18)$$

where v_∞ is the asymptotic incoming speed of the fluid, c is the speed of light, and $u^{i'} = u^i + \beta^i u^0$ is the normal-frame spatial velocity which is a primitive variable used in the code⁴. Given the sound speed $c_{s,\infty}$, the fluid internal energy density

$$e_\infty = \frac{c_{s,\infty}^2 \rho_\infty}{\Gamma(\Gamma - 1 - c_{s,\infty}^2/c^2)}, \quad (19)$$

and pressure

$$p_\infty = e_\infty(\Gamma - 1), \quad (20)$$

can be initialized accordingly.

We initialize the magnetic field as

$$\bar{B}^i = B_0(0, \sin \theta_B, \cos \theta_B), \quad (21)$$

where B_0 is the field strength and θ_B is the inclination angle between the BH spin and the magnetization of the incoming fluid. $\theta_B = 0$ corresponds to a purely poloidal configuration, i.e. magnetic field of incoming fluid is aligned with the BH spin.

In the asymptotic limit ($x^i \rightarrow \infty$), the magnetic field strength B_0 is related to the magnetization of the fluid σ as

$$\sigma_\infty = \frac{(b^2)_\infty}{(\rho c^2 + e + p)_\infty} = \frac{B_0^2/(1 - v_\infty^2/c^2)}{\rho_\infty c^2 + \Gamma e_\infty}. \quad (22)$$

The plasma β -parameter and the magnetization σ are related via

$$\beta_\infty = \frac{p_{\text{gas}}}{p_b} = \frac{p_\infty}{(b^2)_\infty/2} = \frac{2(c_{s,\infty}/c)^2}{\Gamma \sigma_\infty}. \quad (23)$$

Input parameters of our simulations are the asymptotic fluid mass density ρ_∞ , accretion radius R_a , asymptotic sound speed $c_{s,\infty}$, the plasma parameter β_∞ , and

² This definition of the magnetic field is not covariant, as it is different by a factor of α (the lapse function in 3+1 decomposition) from the Eulerian magnetic field B^i commonly adopted in numerical relativity or relativistic electrodynamics literature [e.g. 54–56]. However, we adopt the definition (16) here since it simplifies the handling of the solenoidal constraint on the magnetic field as,

$$\partial_i \bar{B}^i = 0,$$

in the Kerr-Schild coordinates.

³ <https://github.com/IAS-Astrophysics/athenak>

⁴ See the Sec. 4 of Ref. [57] for the definition of GRMHD primitive variables used in ATHENA++.

TABLE I. List of the models and parameters considered in this work. Each column denotes the accretion radius R_a , asymptotic fluid incoming speed v_∞ , asymptotic Mach number \mathcal{M} , accretion time scale τ_a , the plasma beta parameter of the incoming fluid β_∞ , and the magnetic field inclination angle θ_B .

Label	R_a [r_g]	v_∞/c	\mathcal{M}	τ_a [r_g/c]	β_∞	θ_B	Comments
$\beta_{10}\text{-}\theta_{90}\text{-}R_{200}$	200	0.1	2.0	2000	10	90°	Fiducial setup
$\beta_{10}\text{-}\theta_{68}\text{-}R_{200}$	200	0.1	2.0	2000	10	67.5°	Varying θ_B
$\beta_{10}\text{-}\theta_{45}\text{-}R_{200}$	200	0.1	2.0	2000	10	45°	
$\beta_{10}\text{-}\theta_{23}\text{-}R_{200}$	200	0.1	2.0	2000	10	22.5°	
$\beta_{100}\text{-}\theta_{90}\text{-}R_{200}$	200	0.1	2.0	2000	100	90°	Weaker magnetization
$\beta_{10}\text{-}\theta_{90}\text{-}R_{50}$	50	0.2	4.0	250	10	90°	Faster speed
$\beta_{10}\text{-}\theta_{90}\text{-}R_{400}$	400	0.07	1.4	5660	10	90°	Slower speed

the magnetic field inclination angle θ_B . The incoming speed of the fluid v_∞ is computed from $v_\infty^2 = 2GM/R_a$ and used to initialize the spatial velocity (18). From the sound speed $c_{s,\infty}$, both internal energy density and pressure can be initialized using (19) and (20). The plasma parameter β_∞ determines the relativistic magnetization σ_∞ via (23), in turn giving B_0 from (22), which we use to initialize the magnetic fields as (21). Primitive variables are initialized everywhere in the computational domain with the values prescribed as above.

Simulation parameters are listed in Table I. We particularly focus on the cases that the magnetic field of the incoming fluid has a toroidal component with respect to the BH spin (see Ref. [52] for the poloidal magnetic field configuration). For all simulations we adopt a BH spin parameter $a = 0.9M$ and the asymptotic sound speed $c_{s,\infty} = 0.05c$. Our representative, fiducial model assumes $\beta_\infty = 10$ with a purely toroidal orientation of the magnetic field $\theta_B = 90^\circ$, along with the fluid incoming speed $v_\infty = 0.1c$ corresponding to $R_a = 200r_g$; this model is labeled as $\beta_{10}\text{-}\theta_{90}\text{-}R_{200}$. To explore the influence of magnetic field orientation relative to the BH spin, we run the identical setup but varying $\theta_B = 22.5^\circ, 45^\circ, 67.5^\circ$, each of which is labeled with θ_{23}, θ_{45} , and θ_{68} . We perform an experiment on the effect of a weaker magnetization $\beta_\infty = 100$ while keeping other parameters fixed from the fiducial model. Lastly, we run two more models with a smaller ($R_a = 50r_g$) and a larger ($R_a = 400r_g$) accretion radius to test the influence of the fluid incoming speed, also keeping the other parameters fixed to the same values as the fiducial model.

C. Analysis

In addition to the magnetohydrodynamics variables evolved on the grid, we compute following integral quantities from simulation data in order to monitor time evolution of the system:

- Mass accretion rate

$$\dot{M} = \oint (-\rho u^r) \sqrt{-g} d\theta d\phi, \quad (24)$$

where ρ is the rest mass density and u^r is the radial component of the four-velocity. Note the minus sign in the integrand, which makes a positive value indicate mass inflow.

- Total energy (in-)flux

$$\dot{E} = \oint T^r_t \sqrt{-g} d\theta d\phi. \quad (25)$$

- Angular momentum (out-)flux

$$\dot{J} = \oint T^r_\phi \sqrt{-g} d\theta d\phi. \quad (26)$$

- Total magnetic fluxes threading the horizon

$$\Phi_{\text{BH}} = \frac{1}{2} \oint_{\text{BH}} |\vec{B}^r| \sqrt{-g} d\theta d\phi. \quad (27)$$

For our discussions presented here and in the following sections, we will often refer to the dimensionless total magnetic fluxes threading the BH horizon

$$\phi_{\text{BH}} \equiv \frac{\Phi_{\text{BH}}}{\sqrt{\dot{M} r_g^2 c}}. \quad (28)$$

The dimensionless magnetic flux can be used as an indicator for the accretion state, showing that for $\phi_{\text{BH}} \gtrsim 20$ jets can be launched [64]. For larger values of ϕ_{BH} , the accretion flow will become fully magnetically arrested [e.g. 64–67].

- Drag force exerted on the BH

$$F^i = -F_{\text{mom}}^i + F_{\text{grav}}^i, \quad (29)$$

where F_{mom}^i is the total momentum (out-)flux through a spherical surface

$$F_{\text{mom}}^i = \oint T^r_i \sqrt{-g} d\theta d\phi, \quad (30)$$

and F_{grav}^i is the gravitational drag computed with a modified Newtonian formula [49, 52]

$$F_{\text{grav}}^i = \int \rho \frac{x^i}{r^3} dV. \quad (31)$$

A minus sign on the right hand side of Eq. (29) accounts for that the momentum loss in a closed volume results in a reaction force to the opposite direction. For example, in our simulation setup in which BH travels to $+x$ direction, $F_{\text{mom}}^x > 0$ corresponds to the deceleration of the BH with respect to the ambient medium, where $F_{\text{grav}}^x > 0$ corresponds to the acceleration.

The flow in the vicinity of the BH is strongly magnetized in our simulations, frequently triggering density and energy floors on troubled grid cells. Since the artificial injection of mass and energy density from numerical flooring can contaminate some of the diagnostics introduced above, we perform surface integrals around the BH at a slightly larger radius than the outer event horizon [e.g. 52]. In our analysis, the horizon magnetic fluxes Φ_{BH} is integrated over the outer event horizon whereas \dot{M} , \dot{E} , \dot{J} , and F_{mom}^i are extracted at $r = 3r_g$. The gravitational drag F_{grav}^i is integrated over the whole volume of the computational domain excluding $r < 3r_g$ in the same regard. We find this approach has no significant effect our diagnostics, see Appendix A for a detailed analysis.

The turbulent nature of the accretion flow leads to high-frequency fluctuations of the time series data. For improved readability, we have averaged all time series data over a sliding time window of $100r_g/c$, unless otherwise stated.

Computations are performed in a scale-free manner by setting $c = GM = \rho_\infty = 1$. We list unit conversions in Appendix B.

III. FIDUCIAL MODEL: JET LAUNCHING FROM TOROIDALLY MAGNETIZED INFLOW

In this section, we analyze the results from the baseline model $\beta_{10}\text{-}\theta_{90}\text{-}R_{200}$ in detail to highlight several key phenomena observed in the simulation. This model features a wind speed $v_\infty = 0.1c$ and a magnetic field in the upstream perpendicular (toroidal) to the black hole spin axis, with its strength set by the plasma parameter $\beta = 10$.

A. Overview

Shortly following the beginning of the simulation, a shocked region around the BH quickly expands and forms a bow-shaped shock front, which is a common characteristic of supersonic BHL accretion flows [e.g. 31, 32, 36, 68]. This initial accretion phase is largely hydrodynamical. Over time, the BH accretes magnetic flux, leading to a build up of a magnetosphere with a surrounding accretion disk. This situation is shown in the time series plots of Fig. 1. We can see that within less than $1,000r_g/c$ ($t \approx 3\tau_a$), the magnetization quickly reaches half-MAD levels, as indicated by the dimensionless magnetic flux ϕ_{BH} , where a magnetically arrested

disk (MAD) state is characterized by $\phi_{\text{BH}} \simeq 50$ [64]. This built-up of magnetic flux coincides with the formation of a magnetized polar funnel region near the black hole. Magnetic field lines near the ergosphere of the BH are increasingly twisted over time due to the frame dragging, and the developing magnetic pressure gradient launches a jetted outflow (Fig. 2).

1. Flow morphology

Figure 2 shows hydrodynamic and magnetic properties of the accretion flow on the meridional (xz) and equatorial (xy) plane at $t = 20400r_g/c \approx 10\tau_a$. Relativistic jets powered by the BH appear as low-density, highly magnetized ($\sigma \gg 1$) funnel regions traversing the shock cone. The wind from the upstream collides with the jets and deflect them downstream with its ram pressure [52]. The amount of jet bending correlates directly with the wind speed (see Fig. 10 and the accompanying discussion).

An accretion disk forms around the BH with the same direction of rotation as the BH spin, and spans out to $r \sim 30r_g$ on the equatorial plane although its spatial extent is varying over time. At the outermost radius of the disk, its circulatory flow is mixed with the regular downstream flow entering the shock cone, forming a stagnation point, as can be seen from the kink-shaped geometry of velocity streamlines (lower left panel of Figure 2). This leads to the bulk motion of the downstream flow being deflected into $-\hat{y}$ direction. In contrast to accretion simulations initialized or supplied with a finite angular momentum (e.g. Fishbone-Moncrief torus [69], or BHL accretion scenarios with a density/velocity gradient [45, 48]), in the case we consider the incoming flow has zero net angular momentum. Spin-induced frame dragging of the BH is the only source of angular momentum imparted onto the flow, naturally limiting the radial size of the accretion disk.

As pointed out in the discussion around Fig. 1, the BH is in a near MAD state [70, 71]. MAD states feature the built-up of strong magnetic flux near the horizon, leading to the establishment of a magnetically arrested flow structure near the innermost stable circular orbit. Once the horizon magnetic flux rises above a threshold, reconnection triggers an ejection of magnetic flux bundles from the BH magnetosphere, accompanied by decay of the horizon magnetic flux [67, 72, 73]. Shearing instabilities, such as the Rayleigh-Taylor instability [74], ultimately trigger a magnetic flux eruption with a simultaneous mass accretion inwards, via interchanging magnetically buoyant low-density bubbles with less magnetized, dense parcel of fluid [75]. Through this process a MAD state is re-established over the viscous timescale of the accretion flow. As a consequence, the BH does not sustain steady outflows but exhibits fluctuations in the jet power and intermittent flux eruptions.

The quasi-periodic MAD cycle results in two notable features in the flow morphology compared to unmagne-

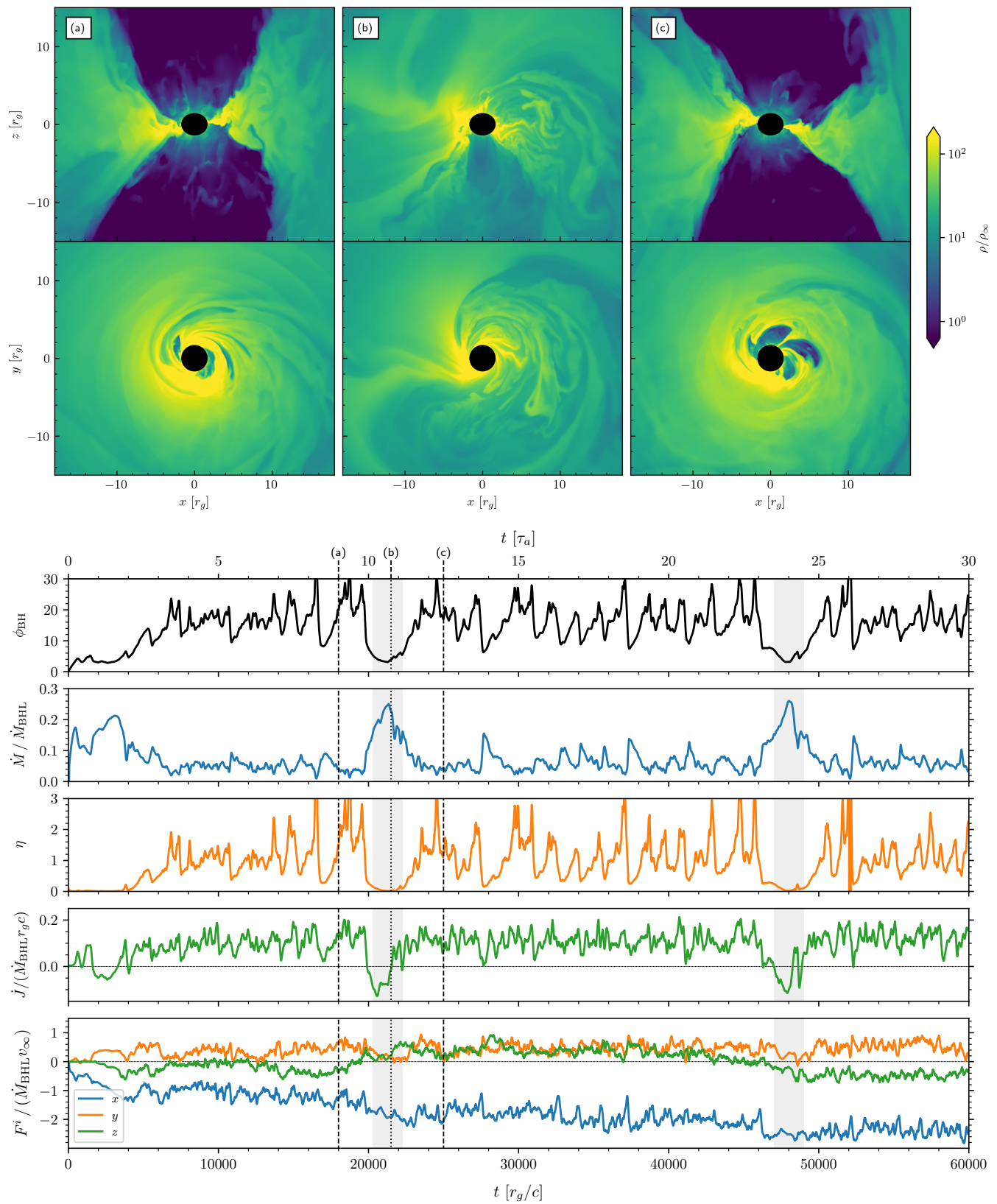


FIG. 1. Time evolution of physical quantities for the representative $(\beta_{10}\text{-}\theta_{90}\text{-}R_{200})$ model. Each panel of the line plots, from top to bottom, presents the dimensionless horizon magnetic flux ϕ_{BH} , mass accretion rate \dot{M} , jet efficiency η , angular momentum flux \dot{J} , and the total drag force F^i . Quiescent periods (shaded) with a duration $\sim 2000M$ are separated by an epoch of continued flux eruptions lasting $\sim 24000M$. Color plots on top of this figure show the mass density, ρ , on the xz (first row) and xy (second row) plane in active states $t_{(a)} = 1.8 \times 10^4 r_g/c$, $t_{(c)} = 2.5 \times 10^4 r_g/c$ and a SANE-like quiescent state $t_{(b)} = 2.15 \times 10^4 r_g/c$, which are indicated with dashed and dotted vertical lines in the line plots.

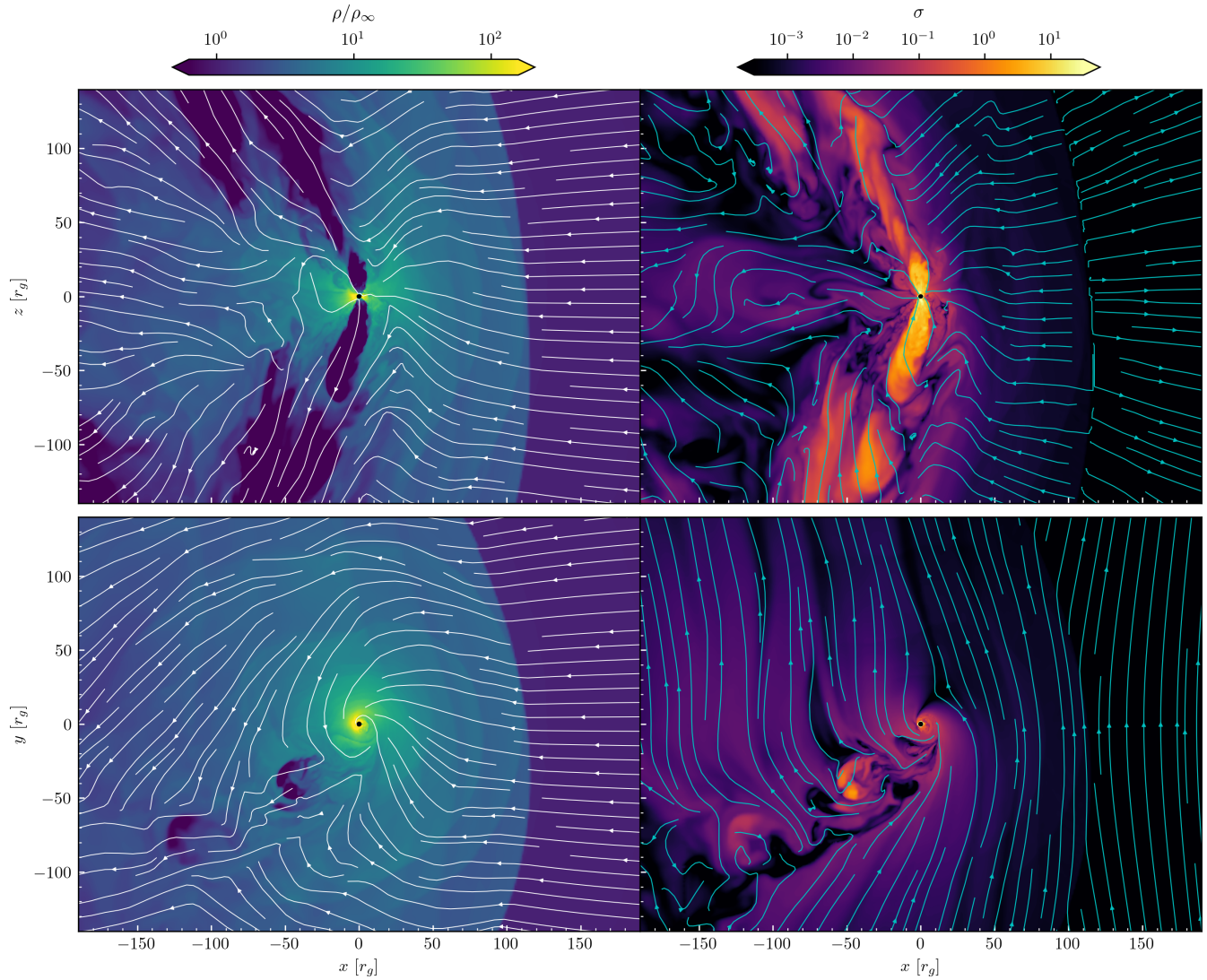


FIG. 2. Transient jets and magnetic flux eruptions in GRMHD Bondi-Hoyle-Lyttleton accretion. Shown here are mass density, ρ , (left) and relativistic magnetization, σ , (right) on the meridional plane (top) and the equatorial plane (bottom) from the fiducial model $\beta_{10}\text{-}\theta_{90}\text{-}R_{200}$ at $t = 20,400 r_g/c$. The in-plane velocity and magnetic fields are shown with white and cyan streamlines on the left and right panels, respectively.

tized axisymmetric BHL accretion flows.

- (1) Each eruption event launches a pressure wave that expands outward from the black hole. This wavefront with a relatively higher density pushes the boundary of the bow shock further upstream, expanding the shock cone, before it shrinks back due to the ram pressure of the incoming fluid. As a consequence, the bow shock exhibits a breathing motion in lockstep with each of the magnetic flux eruptions. This results in a deformed morphology of the shockfront, rather than a smooth parabolic shape commonly observed from unmagnetized cases [e.g. 42, 44, 51, 68]. This eruption-driven expansion of the bow shock and multiple pressure waves approaching the bow shock can be seen from the left panels of Figure 2 or in Figure 4.
- (2) A series of magnetic flux tubes with high magnetization are formed near the BH and drift downstream on the equatorial plane as they are released, a few of which can be identified from the region $x < 0$, $y < 0$ in the lower panels of Figure 2. This situation is reminiscent of unboosted MAD BH flows [e.g. 67, 73, 76]. When a flux eruption event occurs, magnetic pressure pushes the matter outward via an interchange instability and forms highly magnetized, hot, low-density voids near the horizon (e.g. see the simulation snapshots included in Figure 1 and Figure 3). The ejected flux tubes are spiralling outwards from the BH [76], getting sheared and ultimately reach the stagnation point, where they are fragmented by ram pressure and released into the downstream flow as a mushroom-shaped feature. In magnetic flux eruptions of axially symmetric accretion flows, flux tubes would have been launched without a preferred direction. Here, due to a preferential direction of the ambient flow, the flux tubes can be only released toward a particular range of angle relative to the direction of the upstream wind. The ejected flux tubes are filled with hot non-thermal plasma produced by the near-horizon magnetic reconnection that initially created the tubes [72, 73]. This plasma has the potential to power TeV and X-ray flares [76, 77], in a similar manner to what has been proposed as an explanation for galactic flares near Sgr A* [78].

2. Time evolution

Having described the overall properties of the accretion flow, we now focus on its time variability. In Figure 1, we provide the time series data of the dimensionless horizon magnetic flux ϕ_{BH} , mass accretion rate \dot{M} , jet efficiency $\eta = (\dot{M} - \dot{E}/c^2)/\dot{M}$, (outwards directed) angular momentum flux \dot{J} , and the total drag force F^i . Based on these,

we examine the time evolution of our fiducial accretion flow setup in this section.

After the initial development of relativistic polar outflows from the BH ($t \sim 3\tau_a$), the accretion flow undergoes an oscillatory MAD cycle showing a transient behavior of ϕ_{BH} associated with episodes of magnetic flux eruptions. In active phases, when the jet is present, the mass accretion rate is suppressed, whereas it is enhanced in quiet (accreting) phases when the jet is absent. Angular momentum transport in the disk is driven by magnetic flux eruption events, leading to an outward transport of angular momentum, \dot{J} , which is interrupted only briefly when the BH enters the accreting phase [67]. The overall evolution observed in this model is broadly consistent with previous studies on MADs [e.g. 64, 66, 67, 76]. The continued eruption cycle is maintained until $t \sim 10\tau_a$, which we hereafter refer to as the first eruption epoch.

Following the final flux eruption of the first eruption epoch at $t \sim 10\tau_a$, the magnetic flux of the BH drops and the system enters a fully quiescent period, $10\tau_a \leq t \leq 12\tau_a$ with the jet being fully quenched. The accretion flow temporarily enters a standard and normal evolution [SANE, 79] regime. As a result, the mass accretion rate is notably increased and the BH experiences a temporary spin up ($\dot{J} < 0$) from the falling matter.

In the middle of the SANE-like quiescent period, the horizon magnetic flux and the jet efficiency rises again, mass accretion decreases, and the angular momentum flux transitions from inflow (−) to outflow (+). The evolution of the system in this time window is similar to the process of the first jet launching phase, indicating the revival of it. This revival process takes roughly a viscous time scale of the disk. The system re-enters the MAD state and the jet is launched again at $t \sim 12\tau_a$, which marks the beginning of the second eruption epoch lasting $12\tau_a \leq t \leq 23\tau_a$.

In the upper half of Figure 1, we include simulation snapshots displaying the mass density distribution of the accretion flow at three different times $t_{(a)} = 1.8 \times 10^4 r_g/c$, $t_{(b)} = 2.15 \times 10^4 r_g/c$, and $t_{(c)} = 2.5 \times 10^4 r_g/c$, each of which corresponds to (a) an active state by the end of the first eruption epoch, (b) a fully quiet state with no jet present, and (c) an active state in the second eruption epoch after the revival. In the quiet state (b), magnetized polar funnels are replaced by a smooth inflow of matter toward the black hole resembling the SANE accretion state, despite almost uniform distribution of mass density encompassing the BH. This process overall repeats periodically.

B. Magnetic flux eruptions

In the preceding sections, we have described the global dynamics leading to the establishment of a MAD accretion state and subsequent magnetic flux eruption events. In the following, we provide a detailed description of the flux eruption event at $t = 16500 r_g/c$ as a representative

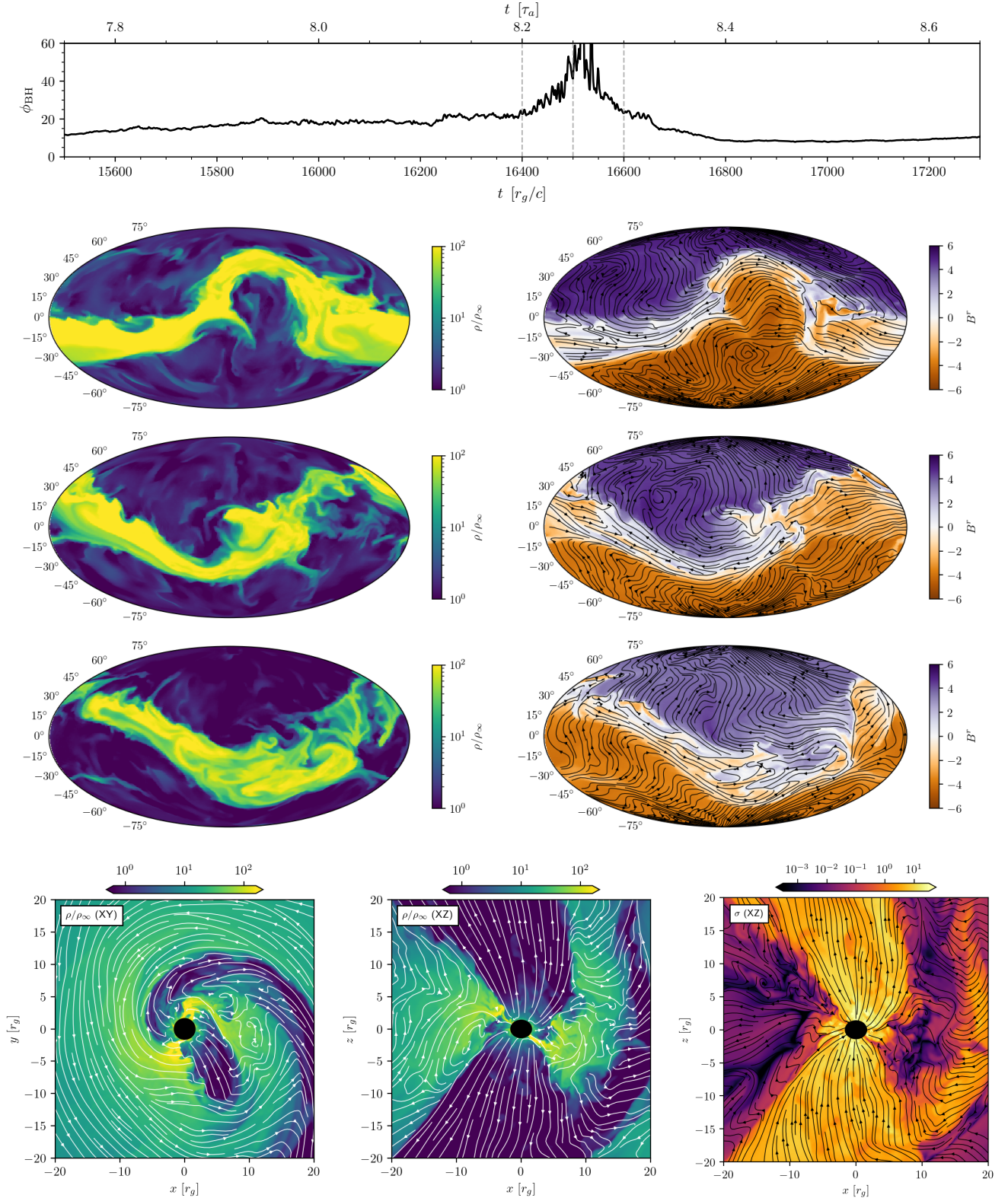


FIG. 3. A magnetic flux eruption event at $t = 16500 r_g/c$. Top panel: change of dimensionless magnetic flux ϕ_{BH} on the black hole (BH) over the eruption. Three vertical dashed lines mark $t = 16400, 16500, 16600 r_g/c$ respectively. Data points are displayed without smoothing. Middle panels: mass density, ρ , (left) and radial magnetic field, B^r , (right) on a spherical surface $r = 5 r_g$ are shown with the Mollweide projection aligned with the BH spin axis. The radial component of the magnetic field is shown in color and the angular components are shown with black streamlines. The center of the plot corresponds to the $+\hat{x}$ direction. From top to bottom, each row corresponds to $t = 16400, 16500, 16600 r_g/c$. Bottom panels: mass density on the equatorial plane (left), on the meridional plane (center), and the relativistic magnetization σ on the meridional plane (right) at $t = 16500 r_g/c$. In-plane velocity and magnetic field are shown with white and black streamlines.

example of the process, and elucidate its effect on the jet morphology. As we will show, the absence of net angular momentum, combined with the purely toroidal accretion flow at large distances, introduces a deviation from the traditional flux eruption dynamics.

1. Near black-hole dynamics

Along with the three sections of plots comprising Figure 3, we now illustrate a comprehensive picture of a single magnetic flux eruption event.

- *Evolution of the horizon magnetic flux* (Figure 3, top panel): The eruption cycle begins with a magnetically relaxed state after the previous eruption has settled down. The horizon magnetic flux ϕ_{BH} starts to increase from $t = 15500r_g/c$, reaching $\phi_{\text{BH}} \approx 20$ at $16300r_g/c$. Then it rapidly rises to $\phi_{\text{BH}} > 50$ around $t = 16500r_g/c$, and relaxes down to $\phi_{\text{BH}} \approx 10$ at $t = 16700r_g/c$ after the eruption.
- *Nutation of the accreting plane* (middle panels in the Mollweide projection in Figure 3): These panels, showing mass density and magnetic field on a spherical surface $r = 5r_g$ at $t = 16400r_g/c$, $16500r_g/c$ and $16600r_g/c$, visualize angular distribution of the accretion flow and the geometry of magnetic field near the BH during the eruption event. In the pre-eruption stage, the accretion disk develops precession with an increasingly large amplitude over time. Left column of the panels shows that the accretion disk is subject to a significant tilt and distortion during the eruption (which otherwise would appear as a smooth strip along the equator). The ejection of the magnetic flux tube during the eruption is off the equator and exerts a strong recoil (and corresponding torque) onto the system, which leads to a nutation of the accretion disk.
- *Tearing of accretion disk* (bottom panels of Figure 3): The asymmetric ejection of the magnetic flux tube (low density/high magnetization region) and the resulting recoil strongly tilting and tearing the inner accretion flow can be clearly seen from the figure. The dynamical time scale of the fluid at which the accretion disk is torn can be estimated via the local Keplerian orbital period as

$$T \approx \frac{2\pi}{\Omega_K} = 2\pi \left(\frac{r^3}{GM} \right)^{1/2} = 370r_g/c \quad (32)$$

for $r = 15r_g$, which is in good agreement with the disk precession period $\approx 400r_g/c$, which we estimate empirically. While the inner part of the accretion disk has a shorter dynamical timescale ($r < 15r_g$) than the driving frequency ($T \approx 400r_g/c$) and is able to reorganize itself, the outer part of the disk with a longer dynamical timescale ($r > 15r_g$) cannot dynamically react (synchronize) to the driving and is

decoupled from the inner part. In a different context, highly tilted accretion disks have been observed to suffer more tearing, precession, and fragmentation, when the inner part of the disk is subject to torque [80].

2. Jet morphology

High-resolution simulations of tilted accretion disks have shown that the motions of the disk and the jet are coupled [80, 81]. The rapid nutation of the accretion disk results in corresponding fluctuations in the direction of the jet launched from the BH. This may (periodically) enhance kink-like instabilities naturally present in these systems [82–85]. From a three-dimensional visualization in Figure 4, one can observe the twisted morphology of the jet associated with the nutation of the accretion plane. While kinks in the jet are clearly visible, at larger distances the interaction with the ambient wind gradually smooths out these features. We can also see how the jet is quenched at a later time.

In Figure 5, we show the distribution of the radially outgoing electromagnetic flux $(T_{\text{EM}})_r^t$ at $r = 100r_g$. The opening angle of the jet shows variations between 15° and 25° , where the position of the peak Poynting flux (center of the jet) precesses with an amplitude $\lesssim 15^\circ$. While the jet still exhibits an oscillatory behavior at this radius to some extent, its angular variations remain much smaller than the inner accretion disk attached to the BH. We expect that these variations will be further attenuated at a larger radius.

C. Drag and spin-down

Here we look into the transport of linear and angular momentum between the BH and the accretion flow, which are responsible for the deceleration and spin-down of the BH.

1. Drag force

An accretor traveling through a gaseous medium is subject to a dynamical friction [86]. The reference scale of this drag is

$$\dot{M}_{\text{BHL}} v_\infty = \pi R_a^2 \rho_\infty v_\infty^2 = \frac{4\pi G^2 M^2 \rho_\infty}{v_\infty^2}. \quad (33)$$

Equation (33) is the drag force in the ballistic (dust) limit, and a multiplicative correction factor needs to be included in generic cases⁵. For convenience, we define

⁵ Newtonian studies suggest that the correction is not expected to exceed a factor of ten in hydrodynamic BHL accretion [31].

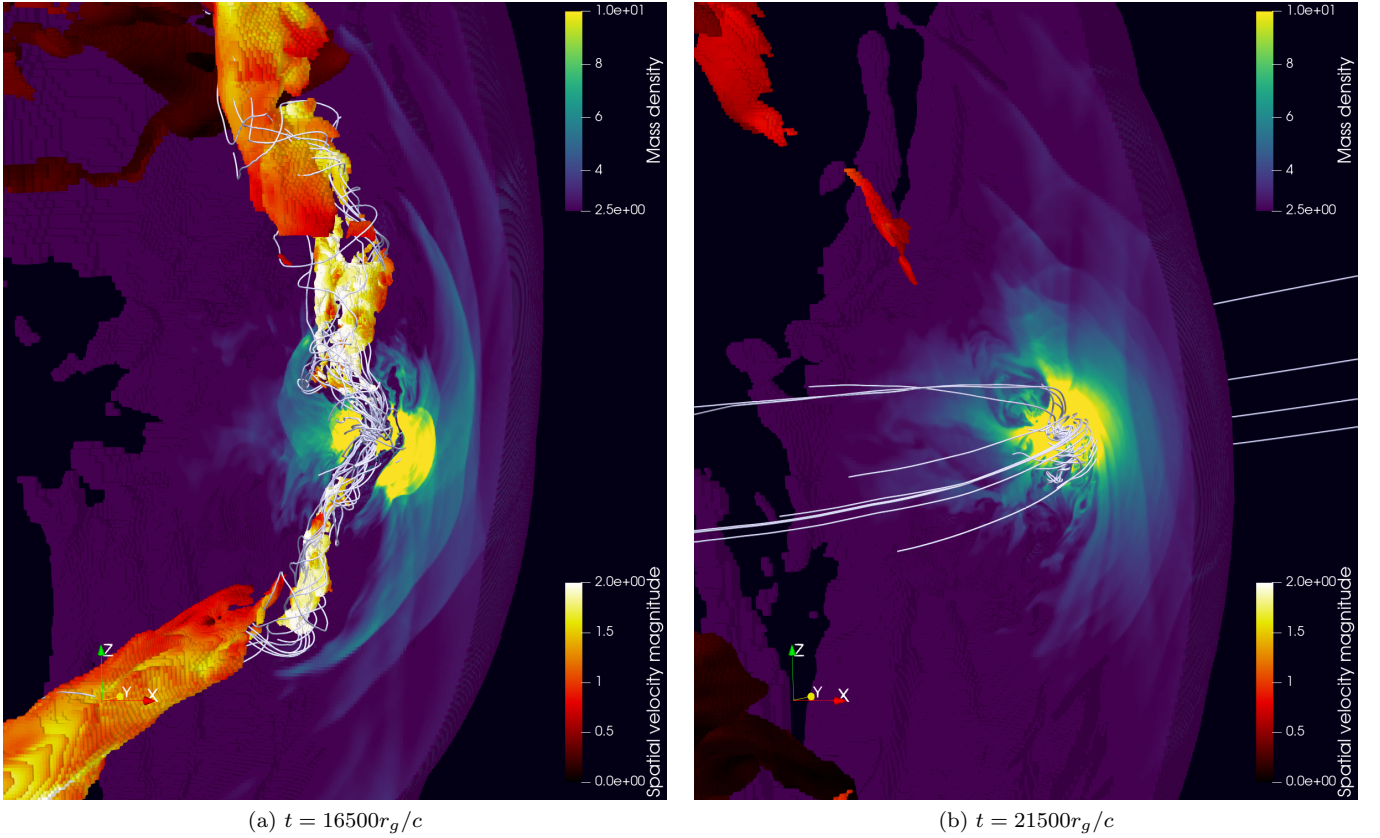


FIG. 4. A three-dimensional rendering of the simulation depicting an active state (left) and a quenched state (right). Shown here are low-density, highly magnetized outflow (filtered by $\rho < 0.05\rho_\infty$, red-white colors), accretion flow inside the bow shock (filtered by $\rho > 2\rho_\infty$ and half-cut to vertical, blue-yellow colors), and magnetic field lines emanating from the accretion disk. Each colormap shows the magnitude of the spatial components of the four-velocity and the normalized mass density ρ/ρ_∞ . A vertical tearing of the accretion disk (see Sec. III B) is visible in the left panel.

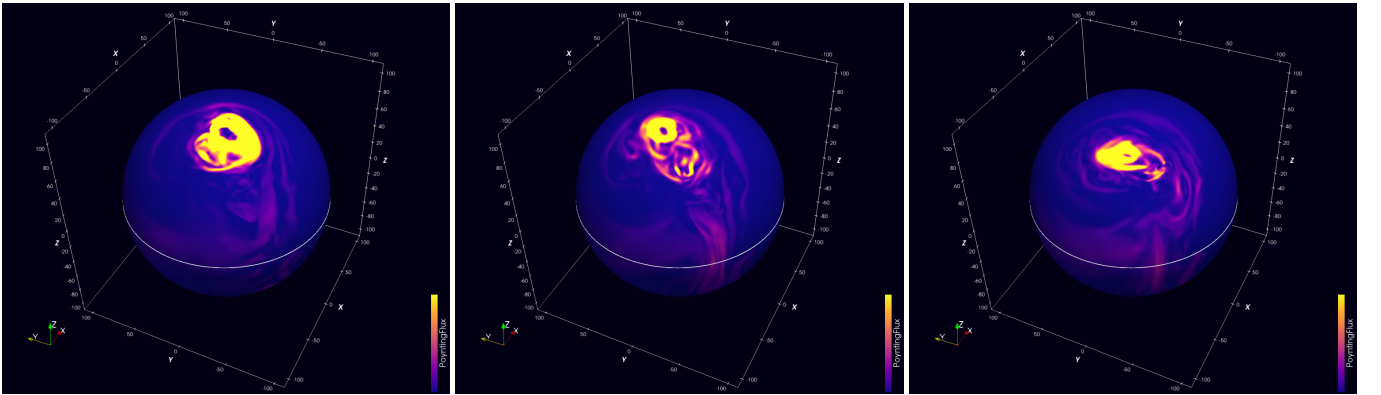


FIG. 5. Distribution of the radial Poynting flux, $(T_{EM})_r^t$, on the upper hemisphere of a spherical surface $r = 100r_g$ at $t = 19600 r_g/c$ (top), $t = 19800 r_g/c$ (center), and $t = 20000 r_g/c$ (bottom).

the fudge factor

$$f_{\text{BHL}}^i \equiv F^i / (\dot{M}_{\text{BHL}} v_\infty) \quad (34)$$

where F^i is the measured drag force in each directions. Since our simulation is performed in a fixed spacetime and does not consistently capture the slow-down of the

BH in dynamical general relativity, the drag force is estimated by means of an approximate formula Eq. (29).

The bottom panel of Figure 1 shows the time variation of the total drag force normalized with the BHL drag scale (33), effectively displaying the factor f_{BHL}^i for each spatial directions. The tangential drag (dynamical

friction) reaches a steady value of $f_{\text{BHL}}^x \sim 2.5$ around $t = 5 \times 10^4 r_g/c$. The linear momentum accretion rate F_{mom}^x is nearly zero when time averaged, yet it is very oscillatory. It is the gravitational drag F_{grav}^x that constitutes a dominant net portion of the total drag. See Sec. A for the raw time series data of F_{mom}^x and F_{grav}^x . A similar trend is observed for F^y and F^z as well, suggesting that the accretion flow plunging into the BH is mostly symmetric when averaged over time. However, we note that F_{mom}^y shows a small positive average $\sim 0.1 \dot{M}_{\text{BHL}} v_\infty$.

The drag force results in a slow-down of the BH relative to the surrounding medium. The deceleration time scale can be estimated by dividing the initial BH linear momentum by the drag force

$$\begin{aligned} t_{\text{dec}} &= \frac{M v_\infty}{f_{\text{BHL}} (\dot{M}_{\text{BHL}} v_\infty)} \\ &= 2.8 \times 10^4 \left(\frac{f_{\text{BHL}}}{1.0} \right)^{-1} \left(\frac{v_\infty}{1000 \text{ km s}^{-1}} \right)^3 \\ &\quad \times \left(\frac{\rho_\infty}{10^{-10} \text{ g cm}^{-3}} \right)^{-1} \left(\frac{M}{100 M_\odot} \right)^{-1} \text{ yr}, \end{aligned} \quad (35)$$

with $f_{\text{BHL}} \sim 2.5$ in our fiducial simulation.

On top of the drag force F^x tangential to the direction of BH motion, there exist nonzero transverse drag (F^y) and vertical drag (F^z) which are perpendicular and parallel to the BH spin. These drags can potentially induce a deflection or oscillatory features in the trajectory of the accreting BH. The transverse drag force F^y shows an average magnitude $\approx 0.5 \dot{M}_{\text{BHL}} v_\infty$, which is about 20% of the tangential drag F^x . The vertical drag F^z has a similar magnitude as the transverse part F^y . The transverse drag F^y maintains a positive finite value where the vertical drag periodically flips its sign between eruption epochs. Each of these components are intimately related with the gravitational Magnus effect (Sec. V B) and the magnetic reversal of jets (Sec. III D) observed in our simulations.

2. Spin-down

As previously noted, in our setup, the spin effect from the BH is the only physical origin of circulation introduced in the accretion flow. From Figure 1, we see that the angular momentum transport rate from the BH into accretion flows is $\dot{J} \approx 0.1 \dot{M}_{\text{BHL}} r_g c$ during eruption epochs where it is reversed during quiescent periods. Angular momentum in the disk is mainly transported in flux eruption episodes [67], where the overall spin-down of the BH is largely affected by the jet as well [87].

The angular momentum loss timescale of the BH can be estimated as

$$t_J = \frac{J_{\text{BH}}}{\dot{J}} = \left(\frac{\dot{J}}{\dot{M} r_g c} \right)^{-1} \left(\frac{a}{M} \right) \left(\frac{M}{\dot{M}} \right). \quad (36)$$

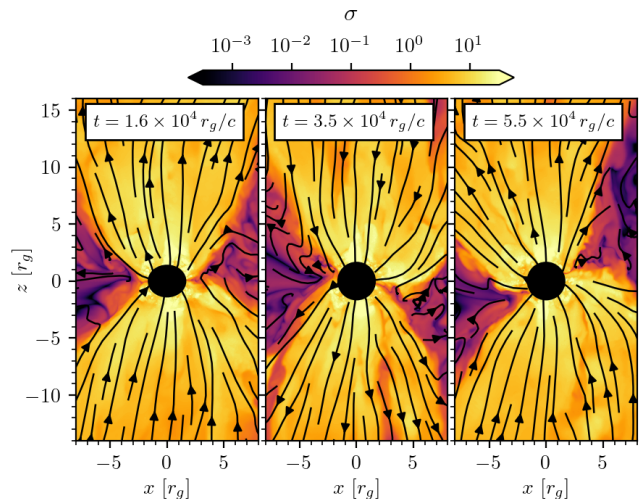


FIG. 6. Magnetic field reversal of the jets between three eruption epochs in the fiducial model with pure toroidal magnetic field in the upstream wind. The relativistic magnetization σ is shown in color and the in-plane components of the magnetic field are shown with black streamlines.

Combined with a measured value $\dot{J}/(\dot{M} r_g c) \sim 2$ in our fiducial simulation during an eruption epoch, Eq. (36) suggest that the spin-down timescale is comparable or shorter than the the mass doubling timescale $t_M \equiv M/\dot{M}$. A systematic investigation on the spin-down of a BH in the MAD state [87] found that the dimensionless spin $J/M^2 = a/M$ decays to $a/M \approx 0.07$ within a characteristic timescale about $t_M/9.5$. Taking $t_J \sim t_M/2$ from our results, the spin-down timescale is

$$\frac{a}{M} = \frac{J}{M^2} \propto \frac{e^{-t/t_J}}{e^{2t/t_M}} \sim e^{-t/(t_M/4)}, \quad (37)$$

yielding a slightly longer timescale than Ref. [87]. This discrepancy can be attributed to the fact that in our case the accretion flow stays in a mildly MAD state for a non-negligible portion of time (see Figure 1).

D. Magnetic reversal

Within the simulation time of the model ($t \leq 6 \times 10^4 r_g/c$), the BH and the accretion flow undergo two quiescent periods at $t = 10\tau_a$ and $t = 24\tau_a$. While all other quantities show a recurring pattern of rise and fall in every eruption epoch, the vertical drag force F^z (see the bottom line plot of Figure 1) shows a distinct behavior in that it flips its sign during a quiescent period and maintains that opposite sign for the next eruption epoch, before coming back to the original sign after another quiescent period.

We find that the polarity of the horizon magnetic fluxes and jets is striped [88] and reversed during these quiescent periods, namely that the MAD state experiences a

magnetic reversal between eruption epochs; see Figure 6. This reversal behavior is observed from all models with a purely toroidal magnetic field ($\theta_B = 90^\circ$) of the incoming fluid. Unfortunately, our simulation is too short to conclusively decide whether the polarity selection always alternates or is stochastic. We postpone a detailed discussion on the origin of this phenomena to future studies.

IV. DEPENDENCE ON ACCRETION PARAMETERS

In this section, we present a systematic survey of the accretion parameters. We change the inclination angle θ_B between the incoming magnetic field and the BH spin (Sec. IV A), then explore a weakly magnetized case with $\beta_\infty = 100$ (Sec. IV B), followed by different incoming speeds of the fluid v_∞ (Sec. IV C). Rather than delving into the same level of detail as the previous section, here we provide a broader overview on qualitative impacts of the physical parameter chosen to be varied.

A. Mixed magnetic fields

Keeping other parameters fixed as the fiducial setup, the inclination angle of the initial magnetic field was varied to $\theta_B = 22.5^\circ, 45^\circ, 67.5^\circ$. The purpose of this experiment is to investigate how much the relative ratio of poloidal to toroidal components of the incoming magnetic field affects jet launching and the time evolution of accretion flow.

In Figure 7, we present the time series data from the three simulations varying θ_B . The result from the fiducial model $\beta_{10}-\theta_{90}-R_{200}$ is overlaid with a transparent line in each panels to highlight deviations from the pure toroidal case. While the overall correlations between each physical quantities is similar to that of the fiducial setup, we compile several observations below.

- (i) The time it takes from the beginning of the simulation to the first successful jet launching and transition to the MAD state is longer for smaller inclination angle, namely when the incoming magnetic field has less toroidal component. The purely toroidal case (θ_{90}) launches the jet the earliest.
- (ii) Within the simulation time $t \leq 5 \times 10^4 r_g/c$, both $\theta_B = 45^\circ$ and $\theta_B = 67.5^\circ$ models did not show any quiescent period; the first eruption epoch continued throughout the final time. In contrast, the $\theta_B = 22.5^\circ$ model turned into a quiescent state after a single eruption epoch of a duration $10\tau_a$, and did not revive its jet activity until the end of the simulation, showing a quiescent period with the duration at least longer than $5\tau_a$. The BH fails to establish a MAD state during this quiescent period, where its episodic launching of weak outflows ($\eta \lesssim 10\%$) into random directions appears to be

very similar to what was observed from low angular momentum accretion flows in Ref. [89–91].

- (iii) However, once the BH enters the eruption (MAD) state, values of ϕ_{BH} , \dot{M} , η and \dot{J} are almost same as the $\theta_B = 90^\circ$ case for all models. This implies that quasi-stationary properties of the MAD state in this setup do not depend on the large scale magnetic field geometry, which only determines the time period between eruption epochs. In Figure 8, we plot the θ_B dependence of the duration of eruption epochs we could observe from our simulations, while we could only constrain lower bounds for $\theta_B = 45^\circ$ and $\theta_B = 67.5^\circ$ cases. Our results indicate a non-monotonic behavior of the eruption epoch duration with the magnetic field orientation θ_B , but an exact functional relationship between them is highly uncertain due to an insufficient number of data points and limited numerical resolution surveys.

B. Lower magnetization

The first column of Figure 9 shows the time series of accretion quantities for the model $\beta_{100}-\theta_{90}-R_{200}$, which has ten times weaker magnetization of the incoming fluid compared to the fiducial model. Several peculiar features observed in this model compelled us to perform a longer time integration up to $t = 8.7 \times 10^4 r_g/c$. We outline those below.

The evolution of the horizon magnetic flux ϕ_{BH} roughly follows a similar cycle. However, it undergoes more gradual increase and fall of ϕ_{BH} between eruption and quiescent periods, exhibiting relatively short duration of eruptions and a longer quiescent period. In other words, the BH cannot sustain the MAD state long enough as the $\beta = 10$ case and takes longer to revive jets once it goes quiescent. This is consistent with the upstream wind providing a smaller amount of magnetic flux per time. The third eruption epoch ($28\tau_a \lesssim t \lesssim 36\tau_a$), though not as conspicuous as the first two, ends up staying only in the mildly MAD regime $\phi_{\text{BH}} \leq 10$. We observe the fourth round of rising magnetic fluxes at $t = 40\tau_a$ during which horizon magnetic fluxes also stayed below $\phi_{\text{BH}} = 10$. In brief, the system exhibits a periodic eruption-quiescence cycle similar to what is observed in our fiducial model, but with a decreasing level of activity over time. We caution that the decay we see may be correlated with numerical resolution and scale separation between the BH and the outer simulation domain boundary.

C. Faster/slower incoming speed

Time evolution of the models with a faster ($R_a = 50r_g$, $v_\infty = 0.2c$) and a slower ($R_a = 400r_g$, $v_\infty = 0.07c$)

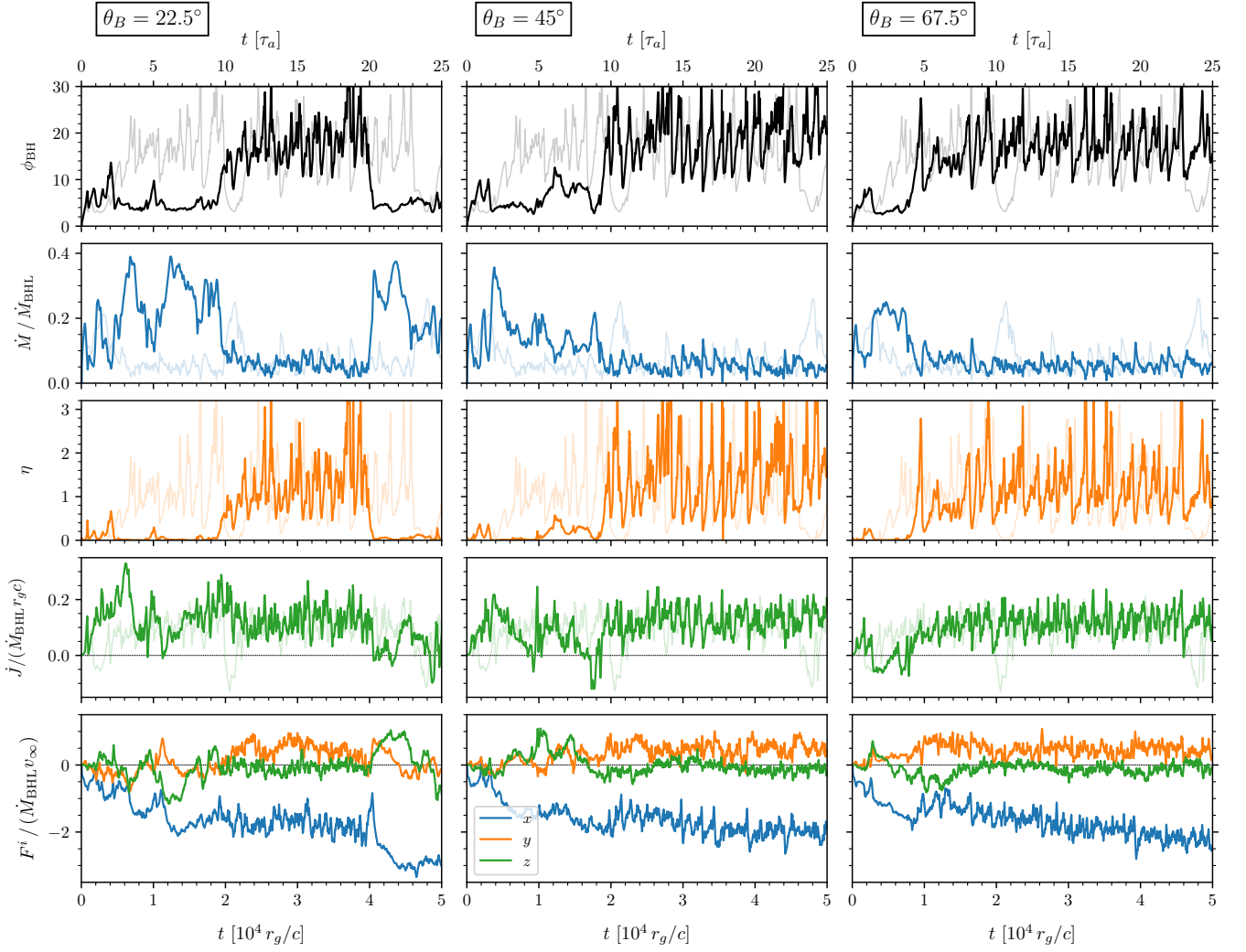


FIG. 7. Time evolution of physical quantities for three models with $\theta_B = 23.5^\circ$, 45° and 67.5° , all with $\beta = 10$ and $R_a = 200$. See Fig. 1 for a description of the quantities shown.

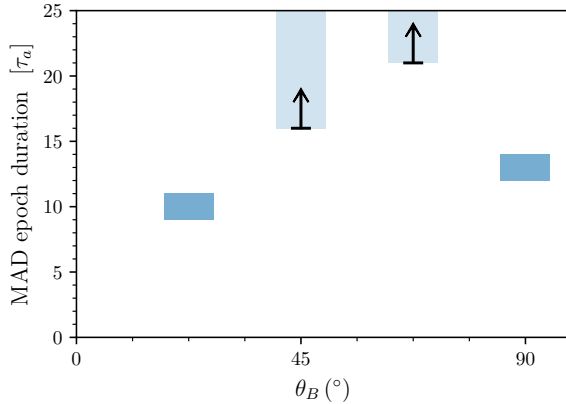


FIG. 8. Duration of a magnetically arrested accretion epoch in units of the accretion timescale $\tau_a = 2000r_g/c$ for the four models with $R_a = 200r_g$ and $\beta_\infty = 10$.

speed of the incoming fluid are shown on the second and third columns in Figure 9. We show the mass density distribution on the meridional plane for the two models in Figure 10, highlighting differences in the shape and radius of the bow shock, as well as the bending angle of outflows from the BH.

We first examine the case with a faster incoming speed ($R_a = 50r_g$). The outflow launched in the polar directions is choked by a strong ram pressure. The BH exhibits sporadic flux eruptions and launches outflows intermittently, but fails to maintain a continuous jet. While the horizon magnetic flux is kept below $\phi_{\text{BH}} \leq 10$, the mass accretion rate shows a large oscillation between 0.3–0.9 \dot{M}_{BHL} , highly anti-correlated with ϕ_{BH} . While the dynamical time of the accretion flow around the BH is the same independent of the wind speed, the replenishing timescale of the flux changes with R_a . For faster wind speeds, the cross section of the bow shock shrinks, with less mass being accreted on the BH, though more

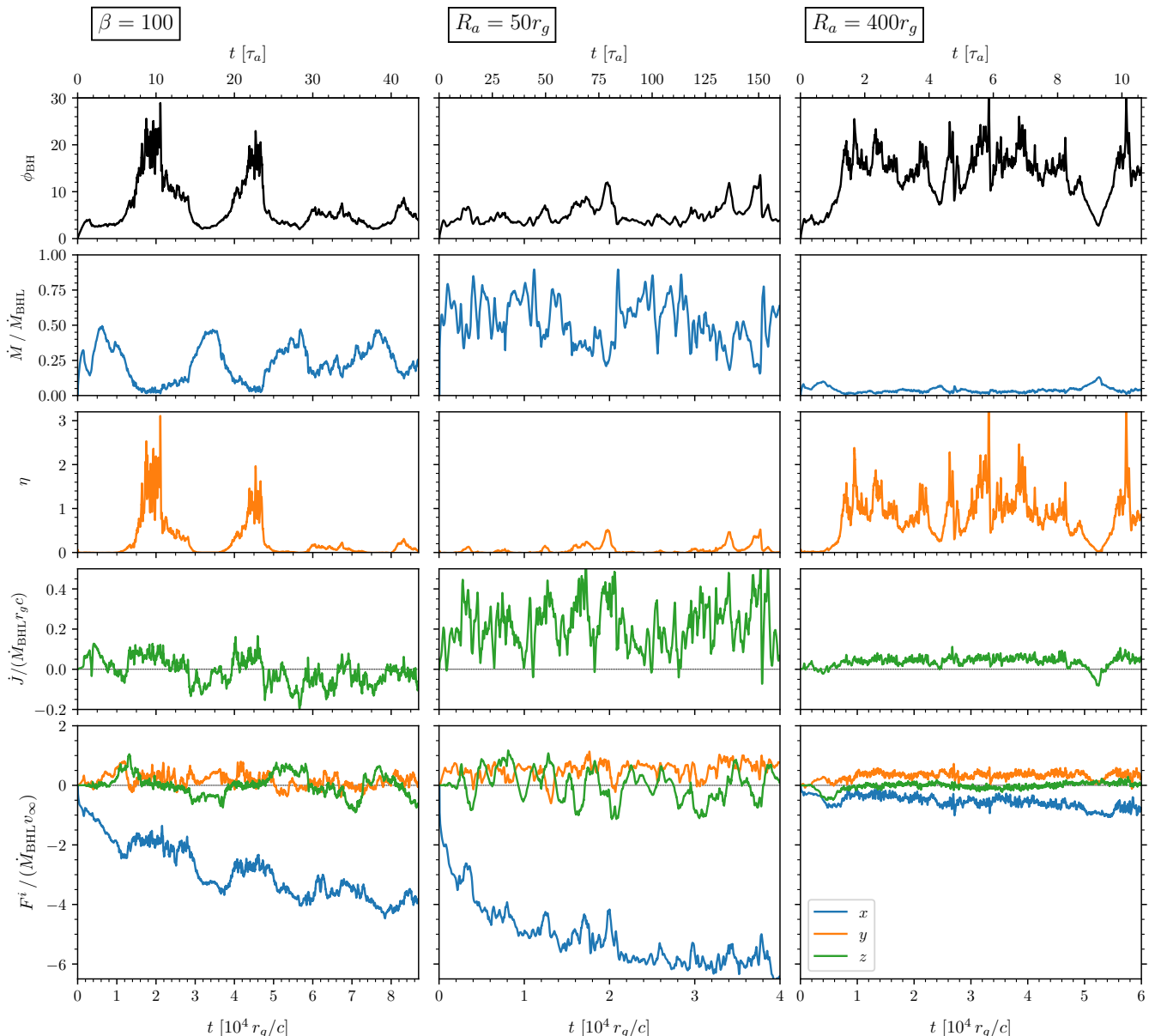


FIG. 9. Time series data for the $\beta_{100}\text{-}\theta_{90}\text{-}R_{200}$ (left), $\beta_{10}\text{-}\theta_{90}\text{-}R_{50}$ (center), and $\beta_{10}\text{-}\theta_{90}\text{-}R_{400}$ (right) models. See Fig. 1 for a description of the quantities shown.

relative to the changed reference rate, \dot{M}_{BHL} . The BH then preferentially accretes in a SANE regime, even if the magnetic properties of the wind at large scales remain the same. This likely implies that questions about flux accumulation on the black hole horizon in BHL accretion cannot be separated from the effective speed of the black hole. We also observe that the tangential drag reaches $f_{\text{BHL}}^x \approx 6$ by the end of the simulation; recall that $f_{\text{BHL}}^x \approx 2.5$ in our fiducial model with $R_a = 200r_g$.

Next, we examine the model with a slower incoming speed of fluid ($R_a = 400r_g$). The accretion flow reaches the MAD state relatively early at $t \sim 1.5\tau_a$. The shorter time for the flow to become magnetically arrested is con-

sistent with the scaling argument presented in [52],

$$\tau_{\text{MAD}}/\tau_a \propto R_a^{-3/4}, \quad (38)$$

while we note the exponent can be slightly different for toroidally magnetized configuration. The accretion flow enters a quiescent period at $t \sim 9\tau_a$ and revives jets at $t \sim 10\tau_a$, also showing a magnetic reversal behavior. The overall time evolution of this model is qualitatively very similar to the fiducial model discussed in Sec. III. The dynamical friction measured by the end of the simulation was $f_{\text{BHL}}^x \sim 1.0$. However, we expect a higher value in practice as the measured value of the drag had not fully reached a steady state during our integration time.

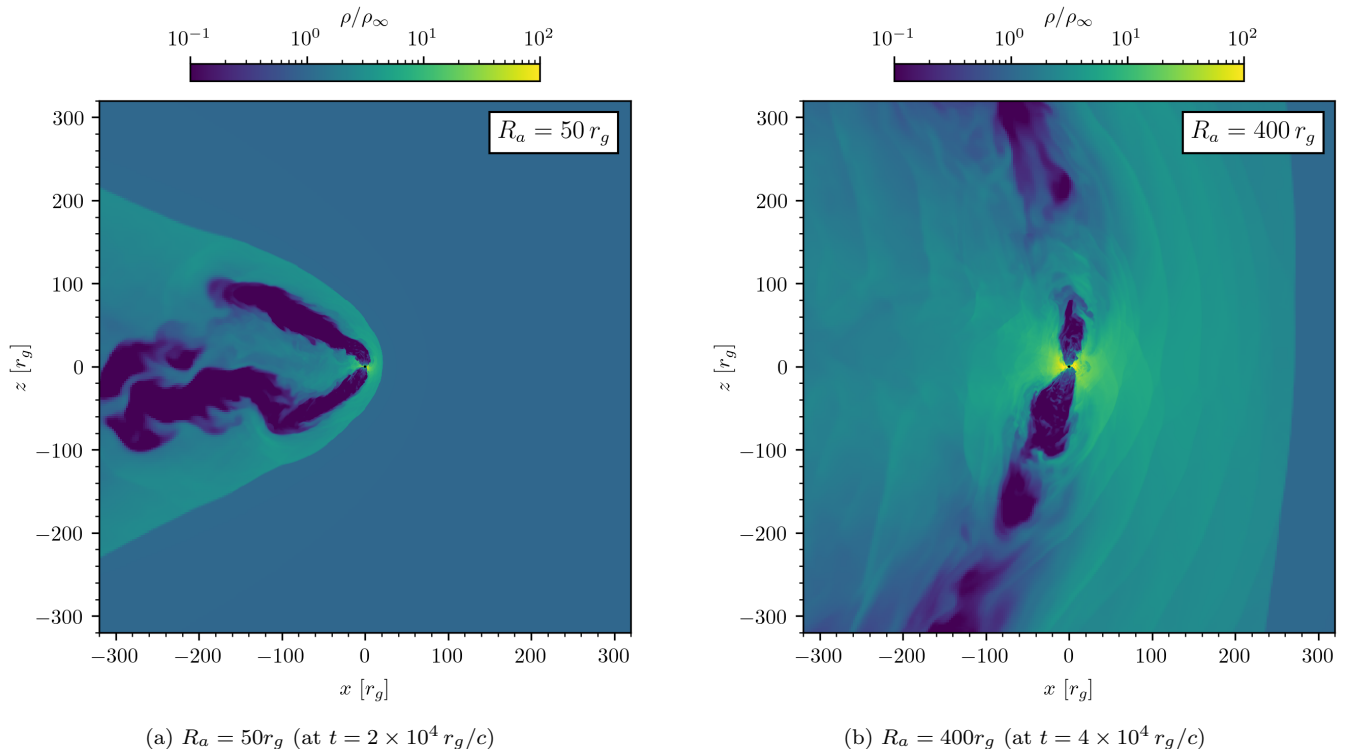


FIG. 10. Distribution of the mass density ρ in the meridional plane for the simulations $\beta_{10}\text{-}\theta_{90}\text{-}R_{50}$ (left) and $\beta_{10}\text{-}\theta_{90}\text{-}R_{400}$ (right). R_a is the accretion radius, r_g is the gravitational radius of the black hole, and ρ_∞ is asymptotic mass density of the wind.

We also observe that the magnitude of the vertical drag is reduced to $|f_{\text{BHL}}^z| \sim 0.1$ and the correlation of its sign and the magnetic polarity of the jet has become weaker compared to the fiducial model. The vertical drag occasionally turns to a positive value during $2.5\tau_a \leq t \leq 4.5\tau_a$ where the direction of magnetic field threading the BH and the jet has been steadily kept to $+\hat{z}$ during the period. Considering that the astrophysically realistic speed of the BH is still much beyond the lower limit of v_∞ explored in this study, it follows that the vertical drag F^z may be effectively uncorrelated or only weakly correlated with the magnetic polarity of jets in realistic situations.

V. DISCUSSION

A. Jet power

Figure 11 compares the jet power $P_{\text{jet}} = \dot{M}c^2 - \dot{E}$ for all models. Once the accretion enters the MAD state, the absolute jet power does not show much dependence on the inclination angle θ_B of the incoming magnetic field. A slight decrease in jet power is observed when the magnetization of the incoming medium is lower, which can be attributed to a reduced supply of magnetic energy to the BH per unit time. Likewise, an increased jet power for a slower speed of incoming fluid can be understood as

that of a slowly moving BH with a large accretion radius, leading to a higher mass accretion rate ($\dot{M}_{\text{BHL}} \propto v_\infty^{-3}$), and consequently a higher rate of magnetic flux injection onto BH, resulting in a more powerful jet (and vice versa).

Our results indicate that among the accretion parameters varied in this study, the jet power is most significantly influenced by the fluid speed v_∞ and to a lesser extent by the magnetization of the incoming matter (note that the BH speed is v_∞ varied by a factor of two at most, where magnetization is set to be ten times weaker in the $\beta = 100$ model). The magnetic field inclination angle θ_B has a negligible impact on the jet power during eruption epochs. However, it largely effects the time evolution and the intermittency of the jet activity, as previously discussed in Sec. IV A.

The finding from this comparative analysis, namely that the BH speed v_∞ is a primary factor in determining the jet power, also aligns with the fact that basic physical scales of the BHL accretion e.g. Eq. (1) (2) (3) possess a strong dependence in v_∞ with the highest power exponent.

A reference scale of the jet power in physical units can

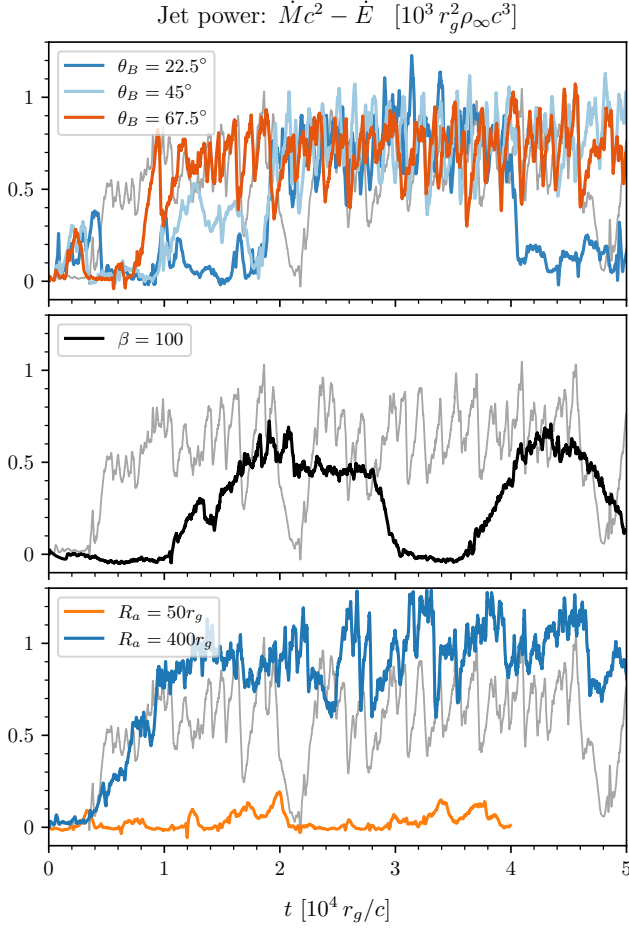


FIG. 11. Jet power $P_{\text{jet}} = \dot{M}c^2 - \dot{E}$ from all simulations. The gray line shows the result from the fiducial model with purely toroidal field. For the scaled efficiency $\eta\dot{M}/\dot{M}_{\text{BHL}}$, see Appendix C

be written as

$$\begin{aligned}
 P_{\text{jet}} &= \eta \left(\frac{\dot{M}}{\dot{M}_{\text{BHL}}} \right) \dot{M}_{\text{BHL}} c^2 \\
 &= 1.0 \times 10^{43} \left(\frac{\eta\dot{M}/\dot{M}_{\text{BHL}}}{0.05} \right) \left(\frac{M}{100M_{\odot}} \right)^2 \\
 &\quad \times \left(\frac{\rho_{\infty}}{10^{-10} \text{ g cm}^{-3}} \right) \left(\frac{v_{\infty}}{1000 \text{ km s}^{-1}} \right)^{-3} \text{ erg s}^{-1}.
 \end{aligned} \tag{39}$$

The factor $\eta\dot{M}/\dot{M}_{\text{BHL}}$ corresponds to an effective energy conversion efficiency with which the rest mass energy inflow $\dot{M}_{\text{BHL}}c^2$ is converted into jet power. Our baseline setup ($\beta_{10}\text{-}\theta_{90}\text{-}R_{200}$) shows the conversion efficiency ≈ 0.05 during an eruption epoch. See Figure 15 in Appendix C for the values of $\eta\dot{M}/\dot{M}_{\text{BHL}}$ from all models.

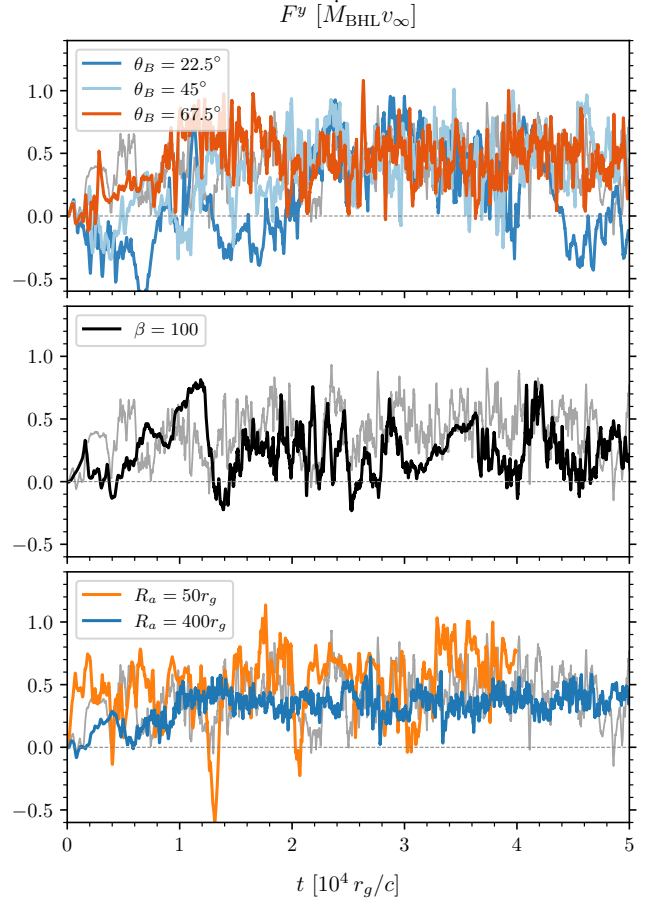


FIG. 12. The drag force to the transverse (y) direction (Magnus force) in all simulations. The gray line shows the result from the fiducial model. A negative value corresponds to the anti-Magnus effect.

B. Magnus effect

As can be seen from Figure 2, the downstream flow trailing the BH is deflected to the $-\hat{y}$ direction owing to the spin of the BH and a resulting circulatory flow surrounding it. This can result in two effects on the transverse drag force F^y : (1) the conservation of linear momentum requires the BH to experience a reaction force to $+\hat{y}$ direction, where (2) since a more amount of matter is deposited to $y < 0$ region of the downstream, a net gravitational pull from the flow is enhanced toward $-\hat{y}$ direction. These two effects are competing with each other, and the direction of the net drag will be highly dependent on the nature of the accretion flow.

A nonzero transverse drag F^y is the manifestation of the (general-relativistic analog of the) Magnus effect, the phenomenon in the classical fluid dynamics that a spinning body moving through a fluid experiencing a drag force normal to both the direction of its motion and spin. Although its physical origin is different, a similar effect is expected to be present in general relativity when a

spinning compact object is immersed in a mass-energy current not aligned with its spin axis [e.g. 38, 92, 93].

However, the precise direction of this gravitational Magnus effect has been under debate when considering non-hydrodynamical types of matter [92–96]. Ref. [93] argues that the gravitational Magnus force consists of two distinctive components (which they name as ‘Magnus’ and ‘Weyl’ respectively therein) and especially the Weyl component can be highly dependent on the specific scenario and boundary conditions of the physical system under consideration. A recent fully relativistic analysis [95] has shown that the drag is always anti-Magnus for a collisionless particle-like matter field, where a wave-like scalar field shows a mixed behavior. A numerical relativity simulation on the BHL accretion of scalar dark matter [96] has reported an anti-Magnus effect.

Ref. [38], to the best of our knowledge, is the only numerical study commenting on this phenomenon in the hydrodynamic regime, and suggested that the enhanced pressure of the accretion flow on the counter rotating side of the Kerr BH gives rise to the (pro-) Magnus effect, albeit without a quantitative argument.

We report in this paper that our physical scenario—3D GRMHD BHL accretion onto a spinning BH—yielded the positive sign of the Magnus force, analogous to the one in classical fluid dynamics. Figure 12 collects and compares the Magnus force F^y from all models. For all the cases, the Magnus drag maintained a positive value for the most of the simulation time. While the gravitational drag force Eq. (31) we compute is not a fully general relativistic formula [see e.g. 93, 95, 96], it is very unlikely to change the direction of the Magnus effect we observe from simulations. We mention that previous numerical studies on the gravitational Magnus effect in a scalar field [92, 96] have been carried out in a boosted metric, unlike our setup in which the black hole is fixed and the inflow is imposed in terms of fluid velocity, potentially causing a quantitative difference in the drag force.

It is also noteworthy that the magnitude of the Magnus force is not small, often rising to a level comparable to the BHL drag force scale $\dot{M}_{\text{BHL}}v_\infty$. Across all models, we quote a conservative overall estimate that the Magnus force has been observed to be about 10% of the dynamical friction. In the circumstances that the initial linear momentum of the BH has been substantially lost by the dynamical friction, its traveling trajectory could have been largely deflected from its original direction of motion.

C. Astrophysical implications

Our results have implications for a number of astrophysical contexts. In an extreme mass-ratio inspiral of binary black hole, if a secondary BH has spin and is surrounded by gaseous medium, the gravitational Magnus force on the secondary can alter its trajectory or excite an eccentricity to the orbit. The resulting features in

gravitational waves can be potentially detectable with next generation gravitational wave detectors e.g. LISA [97]. In the common envelope phase of a binary star, the drag force inside the gaseous envelope is responsible for the orbital decay and expansion of the envelope [98–100]. Our findings imply that the BH orbiting within the envelope could experience the Magnus force when spiralling around the core of the companion star. Depending on the relative orientation of the BH spin to its direction of motion, the Magnus force can increase orbital eccentricity or induce precession of the orbital plane. This may have a considerable impact on the evolution of the BH orbit over long periods and the final configuration of the binary after the common envelope phase. We note that in this context a wind profile varying in the transverse direction needs to be taken into consideration as well, since the nonzero gradient in mass density or velocity leads to a misaligned, rotated shock cone geometry [45, 48, 49] which in turn can significantly alter the direction of the total drag force.

VI. CONCLUSION

We have conducted three-dimensional general-relativistic magnetohydrodynamic simulations of Bondi-Hoyle-Lyttleton accretion onto a spinning black hole when the magnetic field of the surrounding plasma is inclined with respect to the spin of the BH. Our primary motivation was to investigate the dynamics of a BBH merger remnant kicked into the disk of an active galactic nucleus, but owing to the ubiquitous applicability of the Bondi-Hoyle-Lyttleton accretion problem, our results are also applicable to broader astrophysical contexts. We summarize our main findings below.

- The accumulation of magnetic flux onto the BH establishes a magnetically arrested state of the accretion flow and launches relativistic outflows to polar directions, which are bent toward the downstream at a larger radius [52]. The accretion disk surrounding the BH extends up to a few tens of r_g from the horizon, and is encompassed by a large-scale downstream flow in the shock cone.
- Quasi-periodic magnetic flux eruptions from the BH launch pressure waves expanding the bow-shaped shock cone, and release strongly magnetized blobs (flux tubes)—which can potentially power flare-type electromagnetic transients (e.g., [77, 101])—along the equatorial plane into a narrow range of angles relative to the wind direction.
- Anisotropic recoil from the magnetic flux eruptions drive a strong nutation on the accretion disk, often ripping its inner region off from the outer part. Nutation of the accretion disk is imprinted on the jet as its twisted morphology, aiding the development of a kink instability [85].

- For a purely toroidally magnetized wind ($\theta_B = 90^\circ$), the system periodically undergoes a quiescent period with the duration $\gtrsim \tau_a$, during which jet is quenched and the accretion flow relaxes to the SANE state. Magnetic polarity inversion is observed during this period.
- With increasing inclination of the wind magnetization relative to the BH spin (i.e. more toroidal), the jet launched earlier. However, the jet power and efficiency did not show significant differences once the system establishes a MAD state. The orientation of the incoming magnetic field appears to hardly affect steady-state properties of the jet, but determines the temporal behavior of its active and quiescent periods.
- The model with a lower magnetization $\beta = 100$ shows a more gradual evolution of ϕ_{BH} over active and quiescent epochs, as well as a slightly decreased jet power, which can be explained by a reduced supply of magnetic fluxes from the accretion flow.
- When subjected to a faster wind speed, a decreased dynamical cross section and an increased ram pressure on the BH results in the suppression of jet launching. On the other hand, the model with a slower wind speed reached the MAD state earliest relative to the accretion timescale τ_a , which is consistent with a qualitative argument made in [52]. The jet power $\dot{M}c^2 - \dot{E}$ shows the strongest dependency in the wind speed among all parameters considered in this work. This strong dependence of the overall flow dynamics on the wind speed suggests that realistic values of v_∞ will be a crucial element for improved models of GRMHD BHL accretion.
- The gravitational Magnus effect is observed across all models, with the magnitude of a few tens of percents of the reference drag scale $\dot{M}_{\text{BHL}}v_\infty$. The direction of the Magnus force is the same as its classical aerodynamic counterpart.

Whereas the accretion radius R_a adopted in this work has one of the largest values in literature for the general relativistic BHL accretion, it is still considerably far from a realistic condition. In the scenario of a kicked BBH post-merger remnant, the recoil velocity is $\lesssim 200 \text{ km s}^{-1}$ for non-spinning binaries [12] where the spin effects can at most enhance the recoil up to $\approx 4000 \text{ km s}^{-1}$ for ‘superkick’ configurations [102, 103]. Newtonian studies suggest that when a BBH is embedded in a gaseous environment, accretion makes their orbital and spin axes aligned [16, 17], suppressing the superkick configuration. The maximum recoil for a spin-orbit aligned binary estimated from numerical relativity simulations is $\approx 500 \text{ km s}^{-1}$ [104–106].

Our present study opens up a number of different avenues for future work, with several questions still remaining to be answered. First, the jet power can be affected by parameters other than those we have considered here:

the magnitude of the BH spin, and the spin-wind orientation [53], or hydrodynamic parameters such as the adiabatic index and the Mach number, which are known to strongly influence the stability of the shock cone [32]. It would be also intriguing to investigate the inflow with a nonzero net angular momentum [45, 48], which provides a more appropriate scenario for the common envelope phase. The inclusion of radiative effects [41] will also greatly change the dynamics for super-Eddington accretion flows. Future investigations would help constructing a more detailed physical picture of a black hole moving through a magnetized medium, with a better bridging of the scale gaps between currently available numerical models and realistic astrophysical scenarios.

ACKNOWLEDGMENTS

The authors are grateful to James M. Stone, Jacob M. Fields, and Hengrui Zhu for technical support, and to Saavik Ford, James Fuller, Matthew Graham, Barry McKernan, Nicholas Rui, and Alexander Tchekhovskoy for insightful discussions. ERM gratefully acknowledges the hospitality of the Aspen Center for Physics, which is supported by National Science Foundation grant PHY-2210452. The simulations were performed on DOE OLCF Summit under allocation AST198, and on DOE NERSC Perlmutter under grant m4575. Figures in this article were produced using Matplotlib [107], Numpy [108], and Scipy [109] packages.

Appendix A: Extraction radius of density-related integral quantities

As discussed in Sec. IIC, the drift flooring algorithm artificially injects the mass density floor to maintain the comoving magnetization σ below an upper limit σ_{\max} . This often induces spurious increases in the fluid-related integral quantities when computed very close to the BH, where the magnetization is very high.

In Figure 13, we show the mass accretion rate \dot{M} integrated at different radii $r_i = \{r_H, 2r_g, 3r_g, 4r_g, 5r_g\}$ from our representative model ($\beta_{10}\text{-}\theta_{90}\text{-}R_{200}$) where $r_H = r_g(1 + \sqrt{1 - a^2/M^2})$ is the outer horizon radius. It can be clearly seen that the artificial effects from numerical flooring becomes almost absent in $r_i \geq 3r_g$.

Figure 14 shows, for the same set of radii, the \hat{x} component of the momentum drag F_{mom}^x computed at the spherical surface $r = r_i$ and the gravitational drag F_{grav}^x integrated over the whole computational domain except the spherical volume $r < r_i$. The momentum drag settles down to near zero for $r_i \geq 3r_g$. The magnitude of the gravitational drag monotonically decreases for a larger r_i since the region $r < r_i$ is simply excluded from the volume integral. The differences between them are not significant, indicating that the gravitational drag is mostly contributed from $r \geq 5r_g$.

Appendix B: Unit conversion

From simulation results, physical values can be recovered as

$$x^i = r_g \hat{x}^i \quad (\text{B1})$$

$$t = (r_g/c) \hat{t} \quad (\text{B2})$$

$$\rho = \rho_\infty \hat{\rho} \quad (\text{B3})$$

$$\dot{M} = (r_g^2 \rho_\infty c) \hat{M} \quad (\text{B4})$$

$$\dot{E} = (r_g^2 \rho_\infty c^3) \hat{E} \quad (\text{B5})$$

$$\dot{J} = (r_g^3 \rho_\infty c^2) \hat{J} \quad (\text{B6})$$

$$\Phi_{\text{BH}} = (r_g^2 \rho_\infty^{1/2} c) \hat{\Phi}_{\text{BH}} \quad (\text{B7})$$

$$F^i = (r_g^2 \rho_\infty c^2) \hat{F}^i \quad (\text{B8})$$

where hat variables are the results in the (scale-free) code unit.

Appendix C: Energy conversion efficiency

In Fig. 15, we additionally show the jet conversion efficiency relative to BHL accretion rate.

-
- [1] B. P. Abbott *et al.* (LIGO Scientific, Virgo), Observation of Gravitational Waves from a Binary Black Hole Merger, *Phys. Rev. Lett.* **116**, 061102 (2016), arXiv:1602.03837 [gr-qc].
 - [2] B. P. Abbott *et al.* (LIGO Scientific, Virgo), GWTC-1: A Gravitational-Wave Transient Catalog of Compact Binary Mergers Observed by LIGO and Virgo during the First and Second Observing Runs, *Phys. Rev. X* **9**, 031040 (2019), arXiv:1811.12907 [astro-ph.HE].
 - [3] R. Abbott *et al.* (LIGO Scientific, Virgo), GWTC-2: Compact Binary Coalescences Observed by LIGO and Virgo During the First Half of the Third Observing Run, *Phys. Rev. X* **11**, 021053 (2021), arXiv:2010.14527 [gr-qc].
 - [4] R. Abbott *et al.* (KAGRA, VIRGO, LIGO Scientific), GWTC-3: Compact Binary Coalescences Observed by LIGO and Virgo during the Second Part of the Third Observing Run, *Phys. Rev. X* **13**, 041039 (2023), arXiv:2111.03606 [gr-qc].
 - [5] N. C. Stone, B. D. Metzger, and Z. Haiman, Assisted inspirals of stellar mass black holes embedded in AGN discs: solving the ‘final au problem’, *Mon. Not. Roy. Astron. Soc.* **464**, 946 (2017), arXiv:1602.04226 [astro-ph.GA].
 - [6] H. Tagawa, Z. Haiman, and B. Kocsis, Formation and Evolution of Compact Object Binaries in AGN Disks, *Astrophys. J.* **898**, 25 (2020), arXiv:1912.08218 [astro-ph.GA].
 - [7] M. Gröbner, W. Ishibashi, S. Tiwari, M. Haney, and P. Jetzer, Binary black hole mergers in AGN accretion discs: gravitational wave rate density estimates, *Astron. Astrophys.* **638**, A119 (2020), arXiv:2005.03571 [astro-ph.GA].
 - [8] W. Ishibashi and M. Gröbner, Evolution of binary black holes in AGN accretion discs: Disc-binary interaction and gravitational wave emission, *Astron. Astrophys.* **639**, A108 (2020), arXiv:2006.07407 [astro-ph.GA].
 - [9] B. McKernan, K. E. S. Ford, T. Callister, W. M. Farr, R. O’Shaughnessy, R. Smith, E. Thrane, and A. Vajpeyi, LIGO–Virgo correlations between mass ratio and effective inspiral spin: testing the active galactic nuclei channel, *Mon. Not. Roy. Astron. Soc.* **514**, 3886 (2022), arXiv:2107.07551 [astro-ph.HE].
 - [10] K. E. S. Ford and B. McKernan, Binary black hole merger rates in AGN discs versus nuclear star clusters: loud beats quiet, *Mon. Not. Roy. Astron. Soc.* **517**, 5827 (2022), arXiv:2109.03212 [astro-ph.HE].
 - [11] N. Kaaz, S. L. Schröder, J. J. Andrews, A. Antoni, and E. Ramirez-Ruiz, The Hydrodynamic Evolution of Binary Black Holes Embedded within the Vertically Stratified Disks of Active Galactic Nuclei, *Astrophys. J.* **944**, 44 (2023), arXiv:2103.12088 [astro-ph.HE].
 - [12] J. A. Gonzalez, U. Sperhake, B. Bruegmann, M. Hannam, and S. Husa, Total recoil: The Maximum kick from nonspinning black-hole binary inspiral, *Phys. Rev. Lett.* **98**, 091101 (2007), arXiv:gr-qc/0610154.

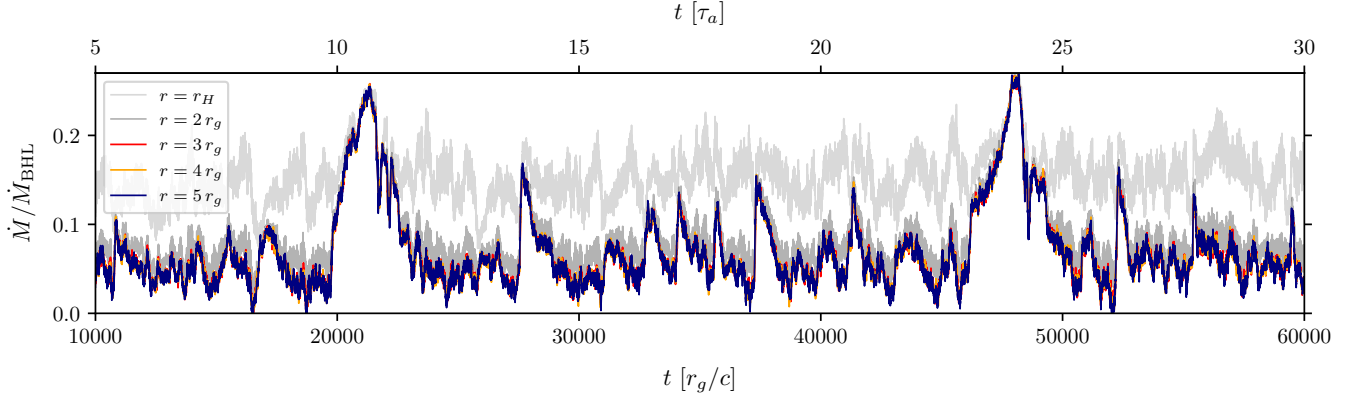


FIG. 13. Mass accretion rate extracted at different radii for the $\beta_{10}\text{-}\theta_{90}\text{-}R_{200}$ model. All data points are displayed without smoothing.

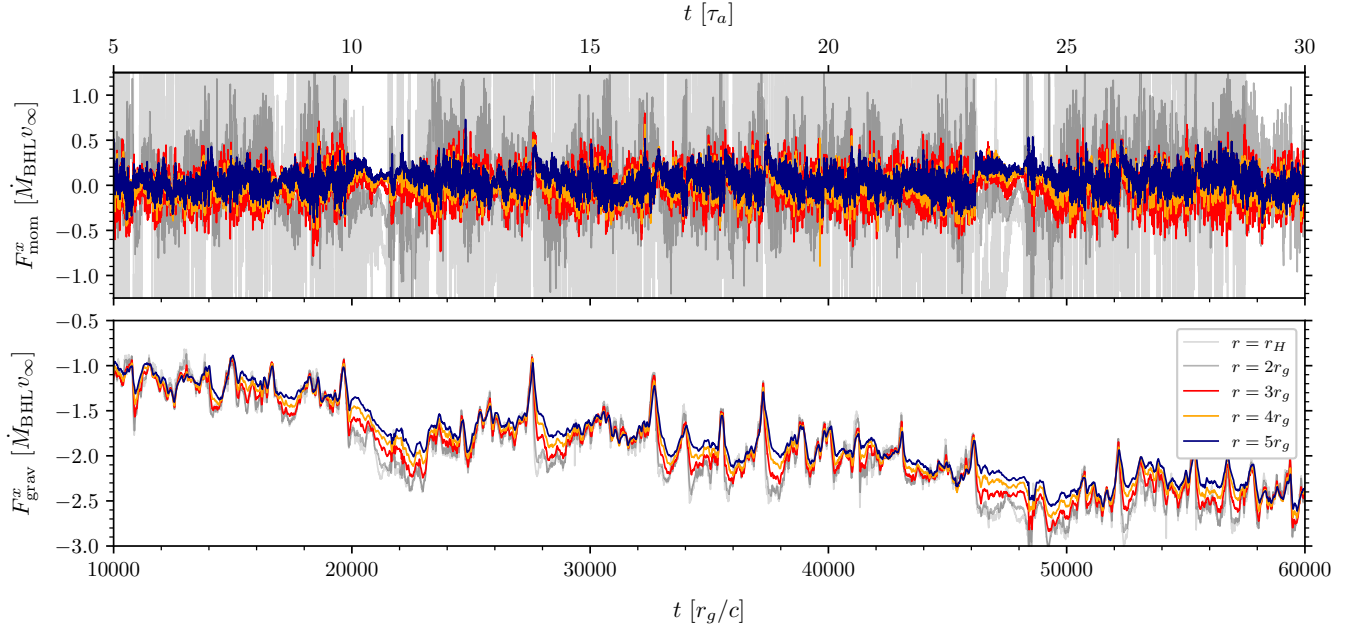


FIG. 14. The \hat{x} component of the momentum drag (top panel) and gravitational drag (lower panel) computed with different radii from the $\beta_{10}\text{-}\theta_{90}\text{-}R_{200}$ model. All data points are displayed without smoothing.

- [13] M. Campanelli, C. O. Lousto, Y. Zlochower, and D. Merritt, Large merger recoils and spin flips from generic black-hole binaries, *Astrophys. J. Lett.* **659**, L5 (2007), arXiv:gr-qc/0701164.
- [14] M. J. Graham *et al.*, Candidate Electromagnetic Counterpart to the Binary Black Hole Merger Gravitational Wave Event S190521g, *Phys. Rev. Lett.* **124**, 251102 (2020), arXiv:2006.14122 [astro-ph.HE].
- [15] K. Chen and Z.-G. Dai, Electromagnetic Counterparts Powered by Kicked Remnants of Black Hole Binary Mergers in AGN Disks, *Astrophys. J.* **961**, 206 (2024), arXiv:2311.10518 [astro-ph.HE].
- [16] T. Bogdanovic, C. S. Reynolds, and M. C. Miller, Alignment of the spins of supermassive black holes prior to merger, *Astrophys. J. Lett.* **661**, L147 (2007), arXiv:astro-ph/0703054.
- [17] M. Coleman Miller and J. H. Krolik, Alignment of supermassive black hole binary orbits and spins, *Astrophys. J.* **774**, 43 (2013), arXiv:1307.6569 [astro-ph.HE].
- [18] A. J. Dittmann, A. M. Dempsey, and H. Li, The evolution of inclined binary black holes in the disks of active galactic nuclei (2023), arXiv:2310.03832 [astro-ph.HE].
- [19] P. F. Hopkins, M. Y. Grudic, K.-Y. Su, S. Wellons, D. Angles-Alcazar, U. P. Steinwandel, D. Guszejnov, N. Murray, C.-A. Faucher-Giguere, E. Quataert, and D. Keres, FORGE'd in FIRE: Resolving the End of Star Formation and Structure of AGN Accretion Disks from Cosmological Initial Conditions, *The Open Journal of Astrophysics* **7**, 18 (2024), arXiv:2309.13115 [astro-ph.GA].

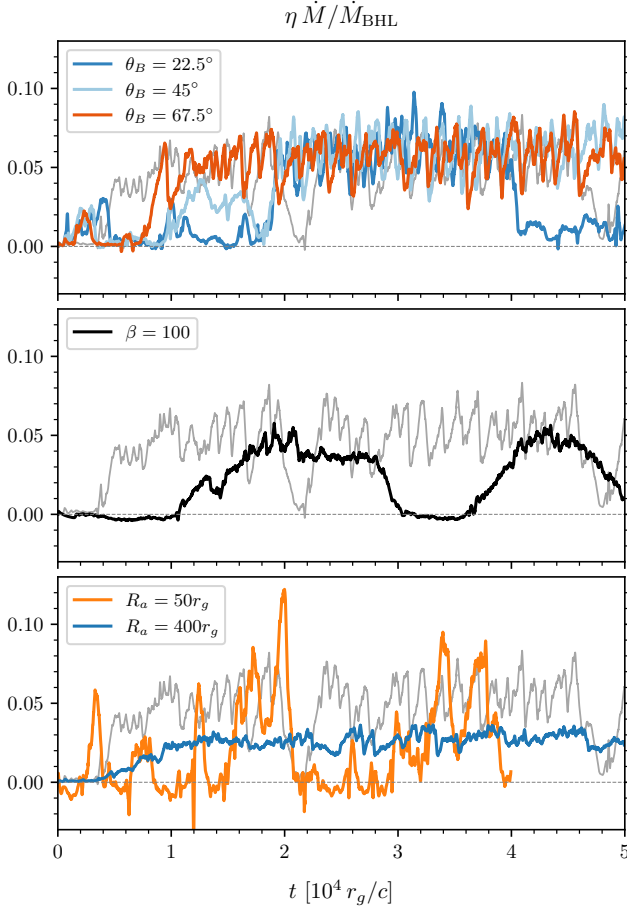


FIG. 15. The (scaled) energy conversion efficiency $\eta\dot{M}/\dot{M}_{\text{BHL}}$ for the jet power. The gray line shows the result from the fiducial model $\beta_{10}\text{-}\theta_{90}\text{-}R_{200}$.

- [20] P. F. Hopkins, J. Squire, K.-Y. Su, U. P. Steinwandel, K. Kremer, Y. Shi, M. Y. Grudic, S. Wellons, C.-A. Faucher-Giguere, D. Angles-Alcazar, N. Murray, and E. Quataert, FORGE'd in FIRE II: The Formation of Magnetically-Dominated Quasar Accretion Disks from Cosmological Initial Conditions, *The Open Journal of Astrophysics* **7**, 19 (2024), arXiv:2310.04506 [astro-ph.HE].
- [21] E. R. Most and H.-Y. Wang, Magnetically Arrested Circumbinary Accretion Flows, (2024), arXiv:2408.00757 [astro-ph.HE].
- [22] H. Bondi, On spherically symmetrical accretion, *Monthly Notices of the Royal Astronomical Society* **112**, 195 (1952).
- [23] F. Hoyle and R. A. Lyttleton, The effect of interstellar matter on climatic variation, *Proceedings of the Cambridge Philosophical Society* **35**, 405 (1939).
- [24] M. MacLeod and E. Ramirez-Ruiz, Asymmetric Accretion Flows within a Common Envelope, *Astrophys. J.* **803**, 41 (2015), arXiv:1410.3823 [astro-ph.SR].
- [25] M. MacLeod, A. Antoni, A. Murguia-Berthier, P. Macias, and E. Ramirez-Ruiz, Common Envelope Wind Tunnel: Coefficients of Drag and Accretion in a Simplified Context for Studying Flows around Objects Embedded within Stellar Envelopes, *Astrophys. J.* **838**, 56 (2017), arXiv:1704.02372 [astro-ph.SR].
- [26] A. Murguia-Berthier, M. MacLeod, E. Ramirez-Ruiz, A. Antoni, and P. Macias, Accretion Disk Assembly During Common Envelope Evolution: Implications for Feedback and LIGO Binary Black Hole Formation, *Astrophys. J.* **845**, 173 (2017), arXiv:1705.04698 [astro-ph.SR].
- [27] D. López-Cámara, E. Moreno Méndez, and F. De Colle, Disc formation and jet inclination effects in common envelopes, *Mon. Not. Roy. Astron. Soc.* **497**, 2057 (2020), arXiv:2004.04158 [astro-ph.HE].
- [28] I. El Mellah, J. O. Sundqvist, and R. Keppens, Accretion from a clumpy massive-star wind in supergiant X-ray binaries, *Mon. Not. Roy. Astron. Soc.* **475**, 3240 (2018), arXiv:1711.08709 [astro-ph.HE].
- [29] N. Kaaz, A. Antoni, and E. Ramirez-Ruiz, Bondi-Hoyle-Lyttleton Accretion onto Star Clusters, *Astrophys. J.* **876**, 142 (2019), arXiv:1901.03649 [astro-ph.HE].
- [30] N. Moeckel and H. B. Throop, Bondi-Hoyle-Lyttleton Accretion onto a Protoplanetary Disk, *Astrophys. J.* **707**, 268 (2009), arXiv:0910.3539 [astro-ph.SR].
- [31] R. G. Edgar, A Review of Bondi-Hoyle-Lyttleton accretion, *New Astron. Rev.* **48**, 843 (2004), arXiv:astro-ph/0406166.
- [32] T. Foglizzo, P. Galletti, and M. Ruffert, A Fresh look at the unstable simulations of Bondi-Hoyle-Lyttleton accretion, *Astron. Astrophys.* **435**, 397 (2005), arXiv:astro-ph/0502168.
- [33] L. I. Petrich, S. L. Shapiro, and S. A. Teukolsky, Accretion onto a moving black hole: An exact solution, *Phys. Rev. Lett.* **60**, 1781 (1988).
- [34] L. I. Petrich, S. L. Shapiro, R. F. Stark, and S. A. Teukolsky, Accretion onto a Moving Black Hole: A Fully Relativistic Treatment, *Astrophys. J.* **336**, 313 (1989).
- [35] E. Tejada and A. Aguayo-Ortiz, Relativistic wind accretion on to a Schwarzschild black hole, *Mon. Not. Roy. Astron. Soc.* **487**, 3607 (2019), arXiv:1906.04923 [astro-ph.HE].
- [36] J. A. Font and J. M. Ibanez, Nonaxisymmetric relativistic Bondi-Hoyle accretion onto a Schwarzschild black hole, *Mon. Not. Roy. Astron. Soc.* **298**, 835 (1998), arXiv:astro-ph/9804254.
- [37] J. A. Font and J. M. Ibáñez, A Numerical Study of Relativistic Bondi-Hoyle Accretion onto a Moving Black Hole: Axisymmetric Computations in a Schwarzschild Background, *Astrophys. J.* **494**, 297 (1998).
- [38] J. A. Font, J. M. Ibanez, and P. Papadopoulos, Non-axisymmetric relativistic Bondi-Hoyle accretion onto a Kerr black hole, *Mon. Not. Roy. Astron. Soc.* **305**, 920 (1999), arXiv:astro-ph/9810344.
- [39] O. Dönmez, O. Zanotti, and L. Rezzolla, On the development of QPOs in Bondi-Hoyle accretion flows, *Mon. Not. Roy. Astron. Soc.* **412**, 1659 (2011), arXiv:1010.1739 [astro-ph.HE].
- [40] O. Dönmez, Relativistic simulation of flip-flop instabilities of Bondi-Hoyle accretion and quasi-periodic oscillations, *Monthly Notices of the Royal Astronomical Society* **426**, 1533 (2012).
- [41] O. Zanotti, C. Roedig, L. Rezzolla, and L. Del Zanna, General relativistic radiation hydrodynamics of accretion flows. I: Bondi-Hoyle accretion, *Mon. Not. Roy. Astron. Soc.* **417**, 2899 (2011), arXiv:1105.5615 [astro-

- ph.HE].
- [42] A. J. Penner, Ultrarelativistic Bondi–Hoyle Accretion I: Axisymmetry, *Mon. Not. Roy. Astron. Soc.* **428**, 2171 (2013), arXiv:1205.4957 [astro-ph.HE].
- [43] F. Koyuncu and O. Dönmez, Numerical simulation of the disk dynamics around the black hole: Bondi Hoyle accretion, *Mod. Phys. Lett. A* **29**, 1450115 (2014).
- [44] F. D. Lora-Clavijo and F. S. Guzman, Axisymmetric Bondi–Hoyle accretion on to a Schwarzschild black hole: shock cone vibrations, *Mon. Not. Roy. Astron. Soc.* **429**, 3144 (2013), arXiv:1212.2139 [astro-ph.HE].
- [45] F. D. Lora-Clavijo, A. Cruz-Osorio, and E. M. Méndez, Relativistic Bondi–Hoyle–Lyttleton Accretion Onto a Rotating Black Hole: Density Gradients, *The Astrophysical Journal Supplement Series* **219**, 30 (2015).
- [46] P. M. Blakely and N. Nikiforakis, Relativistic Bondi–Hoyle–Lyttleton accretion: A parametric study, *Astron. Astrophys.* **583**, A90 (2015).
- [47] A. Cruz-Osorio, F. D. Lora-Clavijo, and F. S. Guzman, Is the flip-flop behaviour of accretion shock cones on to black holes an effect of coordinates?, *Mon. Not. Roy. Astron. Soc.* **426**, 732 (2012), arXiv:1210.6588 [astro-ph.HE].
- [48] A. Cruz-Osorio and F. D. Lora-Clavijo, Non-axisymmetric relativistic wind accretion with velocity gradients on to a rotating black hole, *Mon. Not. Roy. Astron. Soc.* **460**, 3193 (2016), arXiv:1605.04176 [astro-ph.HE].
- [49] A. Cruz-Osorio and L. Rezzolla, Common-envelope Dynamics of a Stellar-mass Black Hole: General Relativistic Simulations, *Astrophys. J.* **894**, 147 (2020), arXiv:2004.13782 [gr-qc].
- [50] A. J. Penner, General Relativistic Magnetohydrodynamic Bondi–Hoyle Accretion, *Mon. Not. Roy. Astron. Soc.* **414**, 1467 (2011), arXiv:1011.2976 [astro-ph.HE].
- [51] M. Gracia-Linares and F. S. Guzman, Accretion of supersonic winds onto black holes in 3D: stability of the shock cone, *Astrophys. J.* **812**, 23 (2015), arXiv:1510.05947 [astro-ph.HE].
- [52] N. Kaaz, A. Murguia-Berthier, K. Chatterjee, M. T. P. Liska, and A. Tchekhovskoy, Jet Formation in 3D GRMHD Simulations of Bondi–Hoyle–Lyttleton Accretion, *Astrophys. J.* **950**, 31 (2023), arXiv:2201.11753 [astro-ph.HE].
- [53] M. Gracia-Linares and F. S. Guzmán, Accretion of supersonic magnetized winds onto black holes, *Mon. Not. Roy. Astron. Soc.* **519**, 6020 (2023), arXiv:2301.04307 [astro-ph.HE].
- [54] T. W. Baumgarte and S. L. Shapiro, *Numerical relativity: solving Einstein's equations on the computer* (Cambridge University Press, Cambridge ; New York, 2010).
- [55] V. Paschalidis and S. L. Shapiro, A new scheme for matching general relativistic ideal magnetohydrodynamics to its force-free limit, *Physical Review D* **88**, 104031 (2013).
- [56] S. S. Komissarov, Electrodynamics of black hole magnetospheres, *Monthly Notices of the Royal Astronomical Society* **350**, 427 (2004).
- [57] J. M. Stone, K. Tomida, C. J. White, and K. G. Felker, The Athena++ Adaptive Mesh Refinement Framework: Design and Magnetohydrodynamic Solvers, *The Astrophysical Journal Supplement Series* **249**, 4 (2020).
- [58] C. R. Trott, D. Lebrun-Grandié, D. Arndt, J. Ciesko, V. Dang, N. Ellingwood, R. Gayatri, E. Harvey, D. S. Hollman, D. Ibanez, N. Liber, J. Madsen, J. Miles, D. Poliakoff, A. Powell, S. Rajamanickam, M. Simberg, D. Sunderland, B. Turcksin, and J. Wilke, Kokkos 3: Programming model extensions for the exascale era, *IEEE Transactions on Parallel and Distributed Systems* **33**, 805 (2022).
- [59] P. Colella and P. R. Woodward, The Piecewise Parabolic Method (PPM) for Gas Dynamical Simulations, *J. Comput. Phys.* **54**, 174 (1984).
- [60] A. Harten, P. D. Lax, and B. v. Leer, On upstream differencing and godunov-type schemes for hyperbolic conservation laws, *SIAM Review* **25**, 35 (1983).
- [61] B. Einfeldt, C. Munz, P. Roe, and B. Sjögreen, On godunov-type methods near low densities, *Journal of Computational Physics* **92**, 273 (1991).
- [62] T. A. Gardiner and J. M. Stone, An Unsplit Godunov Method for Ideal MHD via Constrained Transport in Three Dimensions, *J. Comput. Phys.* **227**, 4123 (2008), arXiv:0712.2634 [astro-ph].
- [63] S. M. Ressler, A. Tchekhovskoy, E. Quataert, and C. F. Gammie, The Disc-Jet Symbiosis Emerges: Modeling the Emission of Sagittarius A* with Electron Thermodynamics, *Monthly Notices of the Royal Astronomical Society* **467**, 3604 (2017), arXiv:1611.09365 [astro-ph].
- [64] A. Tchekhovskoy, R. Narayan, and J. C. McKinney, Efficient Generation of Jets from Magnetically Arrested Accretion on a Rapidly Spinning Black Hole, *Mon. Not. Roy. Astron. Soc.* **418**, L79 (2011), arXiv:1108.0412 [astro-ph.HE].
- [65] J. C. McKinney, A. Tchekhovskoy, and R. D. Blandford, General Relativistic Magnetohydrodynamic Simulations of Magnetically Choked Accretion Flows around Black Holes, *Mon. Not. Roy. Astron. Soc.* **423**, 3083 (2012), arXiv:1201.4163 [astro-ph.HE].
- [66] C. J. White, J. M. Stone, and E. Quataert, A Resolution Study of Magnetically Arrested Disks, *Astrophys. J.* **874**, 168 (2019), arXiv:1903.01509 [astro-ph.HE].
- [67] K. Chatterjee and R. Narayan, Flux Eruption Events Drive Angular Momentum Transport in Magnetically Arrested Accretion Flows, *Astrophys. J.* **941**, 30 (2022), arXiv:2210.08045 [astro-ph.HE].
- [68] E. Shima, T. Matsuda, H. Takeda, and K. Sawada, Hydrodynamic calculations of axisymmetric accretion flow, *Mon. Not. Roy. Astron. Soc.* **217**, 367 (1985).
- [69] L. G. Fishbone and V. Moncrief, Relativistic fluid disks in orbit around Kerr black holes., *Astrophys. J.* **207**, 962 (1976).
- [70] I. V. Igumenshchev, R. Narayan, and M. A. Abramowicz, Three-dimensional mhd simulations of radiatively inefficient accretion flows, *Astrophys. J.* **592**, 1042 (2003), arXiv:astro-ph/0301402.
- [71] R. Narayan, I. V. Igumenshchev, and M. A. Abramowicz, Magnetically arrested disk: an energetically efficient accretion flow, *Publ. Astron. Soc. Jap.* **55**, L69 (2003), arXiv:astro-ph/0305029.
- [72] B. Ripperda, F. Bacchini, and A. Philippov, Magnetic Reconnection and Hot Spot Formation in Black Hole Accretion Disks, *Astrophys. J.* **900**, 100 (2020), arXiv:2003.04330 [astro-ph.HE].
- [73] B. Ripperda, M. Liska, K. Chatterjee, G. Musoke, A. A. Philippov, S. B. Markoff, A. Tchekhovskoy, and Z. Younsi, Black Hole Flares: Ejection of Accreted Magnetic Flux through 3D Plasmoid-mediated Reconnection, *Astrophys. J. Lett.* **924**, L32 (2022),

- arXiv:2109.15115 [astro-ph.HE].
- [74] A. K. Kulkarni and M. M. Romanova, Accretion to Magnetized Stars through the Rayleigh-Taylor Instability: Global Three-Dimensional Simulations, *Mon. Not. Roy. Astron. Soc.* **386**, 673 (2008), arXiv:0802.1759 [astro-ph].
- [75] I. V. Igumenshchev, Magnetically Arrested Disks and Origin of Poynting Jets: Numerical Study, *Astrophys. J.* **677**, 317 (2008), arXiv:0711.4391 [astro-ph].
- [76] O. Porth, Y. Mizuno, Z. Younsi, and C. M. Fromm, Flares in the Galactic Centre – I. Orbiting flux tubes in magnetically arrested black hole accretion discs, *Mon. Not. Roy. Astron. Soc.* **502**, 2023 (2021), arXiv:2006.03658 [astro-ph.HE].
- [77] H. Hakobyan, B. Ripperda, and A. Philippov, Radiative Reconnection-powered TeV Flares from the Black Hole Magnetosphere in M87, *Astrophys. J. Lett.* **943**, L29 (2023), arXiv:2209.02105 [astro-ph.HE].
- [78] J. Dexter *et al.*, Sgr A* near-infrared flares from reconnection events in a magnetically arrested disc, *Mon. Not. Roy. Astron. Soc.* **497**, 4999 (2020), arXiv:2006.03657 [astro-ph.HE].
- [79] R. Narayan, A. Sadowski, R. F. Penna, and A. K. Kulkarni, GRMHD Simulations of Magnetized Advection-Dominated Accretion on a Non-Spinning Black Hole: Role of Outflows, *Mon. Not. Roy. Astron. Soc.* **426**, 3241 (2012), arXiv:1206.1213 [astro-ph.HE].
- [80] M. Liska, C. Hesp, A. Tchekhovskoy, A. Ingram, M. van der Klis, S. B. Markoff, and M. Van Moer, Disc tearing and Bardeen–Petterson alignment in GRMHD simulations of highly tilted thin accretion discs, *Mon. Not. Roy. Astron. Soc.* **507**, 983 (2021), arXiv:1904.08428 [astro-ph.HE].
- [81] M. Liska, C. Hesp, A. Tchekhovskoy, A. Ingram, M. van der Klis, and S. Markoff, Formation of Precessing Jets by Tilted Black-hole Discs in 3D General Relativistic MHD Simulations, *Mon. Not. Roy. Astron. Soc.* **474**, L81 (2018), arXiv:1707.06619 [astro-ph.HE].
- [82] S. Appl, T. Lery, and H. Baty, Current-driven instabilities in astrophysical jets. Linear analysis, *Astron. Astrophys.* **355**, 818 (2000).
- [83] L.-X. Li, Screw instability and blandford-znajek mechanism, *Astrophys. J. Lett.* **531**, L111 (2000), arXiv:astro-ph/0001420.
- [84] R. Narayan, J. Li, and A. Tchekhovskoy, Stability of Relativistic Force-Free Jets, *Astrophys. J.* **697**, 1681 (2009), arXiv:0901.4775 [astro-ph.HE].
- [85] O. Bromberg and A. Tchekhovskoy, Relativistic MHD simulations of core-collapse GRB jets: 3D instabilities and magnetic dissipation, *Mon. Not. Roy. Astron. Soc.* **456**, 1739 (2016), arXiv:1508.02721 [astro-ph.HE].
- [86] S. Chandrasekhar, Dynamical Friction. I. General Considerations: the Coefficient of Dynamical Friction., *Astrophys. J.* **97**, 255 (1943).
- [87] B. Lowell, J. Jacquemin-Ide, A. Tchekhovskoy, and A. Duncan, Rapid Black Hole Spin-down by Thick Magnetically Arrested Disks, *Astrophys. J.* **960**, 82 (2024), arXiv:2302.01351 [astro-ph.HE].
- [88] D. Giannios and D. A. Uzdensky, GRB and blazar jets shining through their stripes, *Mon. Not. Roy. Astron. Soc.* **484**, 1378 (2019), arXiv:1805.09343 [astro-ph.HE].
- [89] S. M. Ressler, E. Quataert, C. J. White, and O. Blaes, Magnetically modified spherical accretion in GRMHD: reconnection-driven convection and jet propagation, *Mon. Not. Roy. Astron. Soc.* **504**, 6076 (2021), arXiv:2102.01694 [astro-ph.HE].
- [90] T. M. Kwan, L. Dai, and A. Tchekhovskoy, The Effects of Gas Angular Momentum on the Formation of Magnetically Arrested Disks and the Launching of Powerful Jets, *Astrophys. J. Lett.* **946**, L42 (2023), arXiv:2211.12726 [astro-ph.HE].
- [91] A. Lalakos, A. Tchekhovskoy, O. Bromberg, O. Gottlieb, J. Jacquemin-Ide, M. Liska, and H. Zhang, Jets with a Twist: The Emergence of FR0 Jets in a 3D GRMHD Simulation of Zero-angular-momentum Black Hole Accretion, *Astrophys. J.* **964**, 79 (2024), arXiv:2310.11487 [astro-ph.HE].
- [92] H. Okawa and V. Cardoso, Black holes and fundamental fields: Hair, kicks, and a gravitational Magnus effect, *Phys. Rev. D* **90**, 104040 (2014), arXiv:1405.4861 [gr-qc].
- [93] L. F. O. Costa, R. Franco, and V. Cardoso, Gravitational magnus effect, *Physical Review D* **98**, 10.1103/physrevd.98.024026 (2018).
- [94] B. Cashen, A. Aker, and M. Kesden, Gravitomagnetic dynamical friction, *Phys. Rev. D* **95**, 064014 (2017), arXiv:1610.01590 [gr-qc].
- [95] C. Dyson, J. Redondo-Yuste, M. van de Meent, and V. Cardoso, Relativistic aerodynamics of spinning black holes, *Phys. Rev. D* **109**, 104038 (2024), arXiv:2402.07981 [gr-qc].
- [96] Z. Wang, T. Helfer, D. Traykova, K. Clough, and E. Berti, Gravitational Magnus effect from scalar dark matter, *Phys. Rev. D* **110**, 024009 (2024), arXiv:2402.07977 [gr-qc].
- [97] N. Afshordi *et al.* (LISA Consortium Waveform Working Group), Waveform Modelling for the Laser Interferometer Space Antenna, (2023), arXiv:2311.01300 [gr-qc].
- [98] M. Livio and N. Soker, The Common Envelope Phase in the Evolution of Binary Stars, *Astrophys. J.* **329**, 764 (1988).
- [99] R. E. Taam and E. L. Sandquist, Common envelope evolution of massive binary stars, *Ann. Rev. Astron. Astrophys.* **38**, 113 (2000).
- [100] N. Ivanova *et al.*, Common Envelope Evolution: Where we stand and how we can move forward, *Astron. Astrophys. Rev.* **21**, 59 (2013), arXiv:1209.4302 [astro-ph.HE].
- [101] V. Zhbankin, B. Ripperda, and A. A. Philippov, Particle acceleration by magnetic Rayleigh-Taylor instability: Mechanism for flares in black hole accretion flows, *Phys. Rev. Res.* **5**, 043023 (2023), arXiv:2302.05276 [astro-ph.HE].
- [102] M. Campanelli, C. O. Lousto, Y. Zlochower, and D. Merritt, Maximum gravitational recoil, *Phys. Rev. Lett.* **98**, 231102 (2007), arXiv:gr-qc/0702133.
- [103] J. A. Gonzalez, M. D. Hannam, U. Sperhake, B. Bruegmann, and S. Husa, Supermassive recoil velocities for binary black-hole mergers with antialigned spins, *Phys. Rev. Lett.* **98**, 231101 (2007), arXiv:gr-qc/0702052.
- [104] F. Herrmann, I. Hinder, D. Shoemaker, P. Laguna, and R. A. Matzner, Gravitational recoil from spinning binary black hole mergers, *Astrophys. J.* **661**, 430 (2007), arXiv:gr-qc/0701143.
- [105] M. Koppitz, D. Pollney, C. Reisswig, L. Rezzolla, J. Thornburg, P. Diener, and E. Schnetter, Recoil Velocities from Equal-Mass Binary-Black-Hole Mergers, *Phys. Rev. Lett.* **99**, 041102 (2007), arXiv:gr-

- qc/0701163.
- [106] J. Healy, C. O. Lousto, and Y. Zlochower, Remnant mass, spin, and recoil from spin aligned black-hole binaries, *Phys. Rev. D* **90**, 104004 (2014), arXiv:1406.7295 [gr-qc].
- [107] T. A. Caswell, A. Lee, E. S. de Andrade, M. Droettboom, T. Hoffmann, J. Klymak, J. Hunter, E. Firing, D. Stansby, N. Varoquaux, J. H. Nielsen, B. Root, R. May, O. Gustafsson, P. Elson, J. K. Seppänen, J.-J. Lee, D. Dale, hannah, D. McDougall, A. Straw, P. Hobson, K. Sunden, G. Lucas, C. Gohlke, A. F. Vincent, T. S. Yu, E. Ma, S. Silvester, and C. Moad, *matplotlib/matplotlib: Rel: v3.7.1* (2023).
- [108] C. R. Harris, K. J. Millman, S. J. van der Walt, R. Gommers, P. Virtanen, D. Cournapeau, E. Wieser, J. Taylor, S. Berg, N. J. Smith, R. Kern, M. Picus, S. Hoyer, M. H. van Kerkwijk, M. Brett, A. Haldane, J. F. del Río, M. Wiebe, P. Peterson, P. Gérard-Marchant, K. Sheppard, T. Reddy, W. Weckesser, H. Abbasi, C. Gohlke, and T. E. Oliphant, Array programming with NumPy, *Nature* **585**, 357 (2020).
- [109] P. Virtanen, R. Gommers, T. E. Oliphant, M. Haberland, T. Reddy, D. Cournapeau, E. Burovski, P. Peterson, W. Weckesser, J. Bright, S. J. van der Walt, M. Brett, J. Wilson, K. J. Millman, N. Mayorov, A. R. J. Nelson, E. Jones, R. Kern, E. Larson, C. J. Carey, Í. Polat, Y. Feng, E. W. Moore, J. VanderPlas, D. Laxalde, J. Perktold, R. Cimrman, I. Henriksen, E. A. Quintero, C. R. Harris, A. M. Archibald, A. H. Ribeiro, F. Pedregosa, P. van Mulbregt, and SciPy 1.0 Contributors, SciPy 1.0: Fundamental Algorithms for Scientific Computing in Python, *Nature Methods* **17**, 261 (2020).